

Article

Dynamic Impact of Urban Built Environment on Land Surface Temperature Considering Spatio-Temporal Heterogeneity: A Perspective of Local Climate Zone

Kaixu Zhao ¹, Mingyue Qi ¹, Xi Yan ¹, Linyu Li ¹ and Xiaojun Huang ^{1,2,3,*}

¹ College of Urban and Environmental Sciences, Northwest University, Xi'an 710127, China; zhaokaixu@stumail.nwu.edu.cn (K.Z.); qimingyue@stumail.nwu.edu.cn (M.Q.); yanxi@stumail.nwu.edu.cn (X.Y.); lilinyu@stumail.nwu.edu.cn (L.L.)

² Shaanxi Key Laboratory of Earth Surface System and Environmental Carrying Capacity, Xi'an 710127, China

³ Shaanxi Xi'an Urban Forest Ecosystem Research Station, Xi'an 710127, China

* Correspondence: huangxj@nwu.edu.cn

Abstract: Thermal environment deterioration has seriously threatened urban habitat quality and urban sustainable development. The evolution of the urban built environment (UBE) is an important cause for urban thermal environment variation. However, the dynamic effect of the UBE on the land surface temperature (LST) is rarely studied by combining the local climate zone (LCZ) theory and spatio-temporal heterogeneity. Based on a case study of Beilin District in Xi'an, China, this paper identified LCZ types of Beilin District in 2010, 2015, and 2020 using the GIS method. It also analyzed the spatial-temporal characteristics of the LST in summer based on the remote sensing retrieval method and explored the effects of the built environment on the LST by Geodetector and geographically weighted regression (GWR). The results showed the following: (1) The area share of dense building zones in Beilin District was greater than that of open building zones and natural surface zones, while the share of mid- and high-rise dense building zones continued to increase and the share of low-rise dense building zones continued to decrease during the study period. (2) The LST of different LCZ types in Beilin District was obviously different, and the LST of dense building zones was generally higher than that of open building zones and natural surface zones. Meanwhile, the LST of mid- and low-rise dense building zones increased gradually, and the LST of high-rise open building zones decreased gradually, but the overall warming area was obviously more than the cooling area. (3) The effects of the UBE factors on the LST varied greatly, with their interaction having an enhancement effect. The direct and interactive influence of the two-dimensional (2D) UBE indicators on the LST were greater than those of the three-dimensional (3D) indicators, but there was a gradual decrease in the force of the 2D indicators and a simultaneous diminution, enhancement, and invariance of the force of the 3D indicators. (4) Vegetation cover (VC) and floor area ratio (FAR) acted negatively, and the building height (BH) was changing from a positive to a negative role, with the average action intensity of VC changing from -0.27 to -0.15 , FAR from -0.20 to -0.16 , and BH from 0.05 to -0.04 . The impervious surface area (ISA), building area (BA), and space congestion (SC) acted positively, with the average action intensity of the ISA changing from 0.12 to 0.20 , BA from 0.12 to 0.19 , and SC was stable at 0.04 . The framework enables a deeper portrayal of LST changes in different LCZs, reflecting the direct and interactive effects of different UBE indicators on LST, as well as local variations in the impact effects and provides a basis for urban managers or planners to improve urban heat resilience.



Citation: Zhao, K.; Qi, M.; Yan, X.; Li, L.; Huang, X. Dynamic Impact of Urban Built Environment on Land Surface Temperature Considering Spatio-Temporal Heterogeneity: A Perspective of Local Climate Zone. *Land* **2023**, *12*, 2148. <https://doi.org/10.3390/land12122148>

Academic Editors: Rajnish Kaur Calay, Lawrence Lau and Isaac Yu Fat Lun

Received: 24 September 2023

Revised: 4 December 2023

Accepted: 7 December 2023

Published: 10 December 2023



Copyright: © 2023 by the authors. Licensee MDPI, Basel, Switzerland. This article is an open access article distributed under the terms and conditions of the Creative Commons Attribution (CC BY) license (<https://creativecommons.org/licenses/by/4.0/>).

Keywords: urban built environment; land surface temperature; urban morphology; spatial heterogeneity; heat island effect; local climate zone

1. Introduction

According to the Sixth Assessment Report of the IPCC, the average global surface temperature has increased by about 1 °C over the past 100 years, and the average global warming is expected to reach or exceed 1.5 °C over the next 20 years [1]. Meanwhile, along with the large-scale urbanization around the world, the rapidly expanding high-density urban form is driving further deterioration of the urban thermal environment and further aggravating the heat island effect [2]. Under the dual influence of global warming and the heat island effect, many environment and health problems have erupted in cities, such as the growing energy consumption [3], aggravated air pollution [4], increased heat-related diseases [5], reduced physical comfort [6], and lost biodiversity [7]. In addition to global warming, the deterioration of the urban thermal environment is largely attributed to the change of the urban built environment (UBE). In the process of continuous urban expansion, a large number of roads and architectural landscapes have replaced ecological spaces such as farmland, forests, and wetlands, which have greatly changed the heat balance of the land surface [8,9]. Exploring the relationship between the UBE and the thermal environment to reduce the urban heat island effect and improve urban thermal resilience has become an important research topic in the field of sustainable urban development.

The urban thermal environment generally includes the canopy thermal environment and the surface thermal environment. The land surface temperature (LST) retrieved from satellite images can be used to represent the surface thermal environment. It has been widely explored due to its higher spatial resolution and closer relationship with the built environment. The current research on the relationship between the UBE and LST is by two main lines. The first is to analyze the influence of the urban two-dimensional (2D) and three-dimensional (3D) built environment on the LST through a regression model. Some valid conclusions from established studies have revealed that normalized difference vegetation index (NDVI) [10,11], normalized difference water index (NDWI) [12,13], building height [14,15], sky view factor [16,17], street canyon aspect ratio [18,19], and floor area ratio (FAR) [20,21] are negatively correlated with the LST. However, the normalized difference built-up index (NDBI) [22,23], impervious surface [24,25], building density [26,27], building volume [28,29], space congestion [28,30], and distribution uniformity [28] are positively correlated with it. Some studies have also pointed out that the building height [31,32], street aspect ratio [33,34], FAR [28,35], and sky view factor [36,37] effectively contribute to LST elevation, and the relationship between the two varies greatly across scales [38,39] and functional areas [40,41], as well as time periods [29,42] and seasons [43,44]. The second is to analyze the difference in the LST among different units by constructing land-use units with different built environments. The local climate zone (LCZ) scheme proposed by Stewart and Oke in 2012 is the most popular, which divides the cities into 10 types of built-up areas (LCZs 1–10) and 7 types of natural cover spaces (LCZs A–G), with the same type of LCZs sharing similar morphological characteristics and temperature attributes [45]. Established studies have shown that the LST of built-up LCZs is generally higher than that of natural-covered LCZs [46–49] at different scales. The LST is typically highest in dense building zones (LCZs 2–3), large low-rise building zones (LCZ 8), and industrial plant zones (LCZ 10), while it is typically lowest in dense wooded zones (LCZ A) and water bodies (LCZ G) [50–54]. These characteristics vary somewhat across time and seasons [55–58], as well as with the proportion of LCZs in a given city and the background climate [59–61].

Despite the rich results obtained, there are still some shortcomings in the research on the relationship between the UBE and LST. First, established studies have not integrated the LCZ scheme deeply into the discussion of the relationship between the UBE and LST. For analyzing the influence of the built environment on the LST through regression modeling, or portraying the LST differences of different land units through the LCZ method, the core logic of both is to explore the relationship between different characteristics of the UBE and LST in the city, except for the difference only in the use of different methodologies. It is objectively necessary to combine the two main lines of research so as to facilitate a more refined portrayal of the relationship between the UBE and LST. A few studies

have made attempts [34,48,62], but more cases are needed. Second, established studies have not explored the changing role of the built environment in influencing the LST in the context of temporal dynamics. The city is an open giant system. Its internal built environment is constantly changing, driving the proportion and composition of the LCZ units to change accordingly, while the intensity of the influence on the LST also fluctuates, so that only by placing it in a longer time dynamics can we discover this law. A few studies, while analyzing the warming and cooling effects of different LCZ units over a long time [63,64], have drawn general conclusions, and they still need to analyze in detail the changes in the influence of different UBE indicators on the LST. Third, established studies have not explored the mechanism of the UBE's influence on the LST based on the spatial heterogeneity. The current studies have their core logic in exploring the role of the built environment on the influence of the LST by global regression with no attention to spatial heterogeneity, whether they are based on linear regression models such as ordinary least squares [65,66], stepwise regression [67,68], multilevel regression [69,70], correlation coefficient [62,71], or on nonlinear regression models such as boosted regression tree [72,73], extreme gradient boosting tree [74,75], and random forest [76,77], or even on spatial regression models such as spatial error, spatial lag, and spatial Durbin [78,79]. A few studies have attempted to apply Geodetector and geographically weighted regression (GWR) to the fields of interest [80,81]. But the two models have their own shortcomings, and how to integrate their applications still needs to be further explored.

Therefore, this paper takes Beilin District in Xi'an City, where there are obvious differences in built environments, as a case site to take spatio-temporal heterogeneity into account. With the data of Landsat remote sensing images, land use, building vectors, road networks, and impervious surfaces, we employed models such as Geodetector and GWR to explore the multidimensional impacts of the urban 2D and 3D built environments on the LST in different periods from the perspective of the LCZ, aiming to clarify the changing rules of the built environment on the thermal environment. This paper focuses on the following questions: (1) How many LCZ types are there in Beilin District of Xi'an, and what are their characteristics and changing trends? (2) What are the characteristics and changing trends of the LST in different LCZs of Beilin District? (3) What are the characteristics and changing trends of the LST in different LCZs of Beilin District based on Geodetector? (4) What are the characteristics and trends of the positive and negative effects and spatial non-stability of the built environment affecting the LST in Beilin District based on GWR, respectively? This study can serve as a reference for urban managers or planning designers to design urban cooling.

2. Materials and Methods

2.1. Study Area

Xi'an is the capital of Shaanxi Province and is a central city in China. In 2020, its built-up area was 942.53 km², and the urban population was 13.16 million. Xi'an has a sub-humid warm temperate continental monsoon climate, with an annual average air temperature of 13.3 °C, an average temperature of 26.5 °C in July, and an annual historical extreme maximum temperature of 43.4 °C. In recent years, the frequency, intensity, and duration of heat waves have been increasing in Xi'an. The number of hot days (daily maximum temperature ≥ 35 °C) in June 2022 exceeded 20 days, making it the hottest June since 1951. Beilin District is one of the administrative districts of Xi'an, located in the city center, with an area of 23.37 km² and residents of 756,800 in 2020. As a typical old urban area with high population density and building density, it carries 13% of the population on less than 1% of the land area in the main urban area of Xi'an. There are only a few green spaces and water sources, such as Xingqing Park, the Small Wild Goose Pagoda, and part of City Wall Park and river. Over the past decade, the further expansion of the Beilin District into two and three dimensions driven by rapid urban construction and renovation has also stimulated an even harsher thermal environment, resulting in a large urban population

facing serious health risks in the thermal environment. It can be used as a typical area to study the relationship between the UBE and LST (Figure 1).

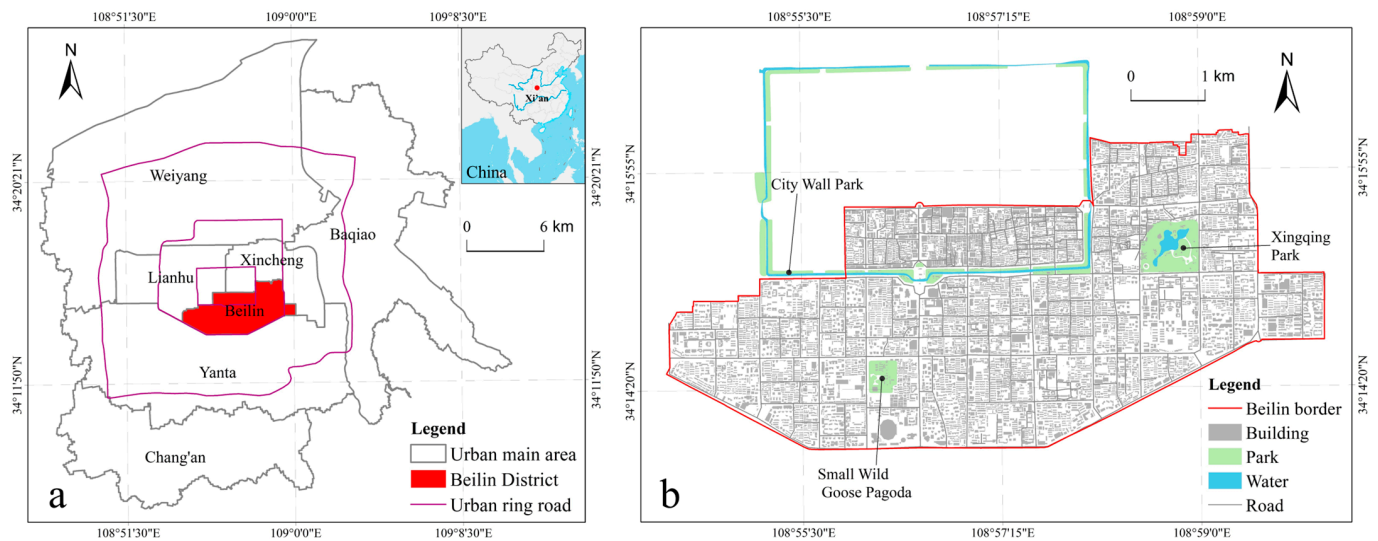


Figure 1. Study area. (a) Location of Xi'an and Beilin District; (b) built environment elements in Beilin District.

2.2. Data Source and Processing

2.2.1. Land Surface Temperature

Land surface temperature is an important indicator to measure the surface thermal environment, which can be acquired by the inversion of a variety of remote sensing products, such as MODIS, Landsat, ECOSTRESS, and Sentinel 3A/3B. Due to the small area of Beilin District, Landsat images with higher spatial resolution were selected for LST inversion, with a resolution of $30\text{ m} \times 30\text{ m}$. In order to show the changes of thermal environment in Beilin District, remote sensing images during summer daytime in 2010, 2015, and 2020 were used (Table 1).

Table 1. Remote sensing image types and basic information.

Satellite Image	Date	Time	Air Temperature	Cloud Cover (%)	Data Source
Landsat 5 TM	17 June 2010	11:10 (CST)	37 °C (max)	1	USGS, https://earthexplorer.usgs.gov/ (20 January 2022)
Landsat 7 ETM+	25 July 2015	11:19 (CST)	36 °C (max)	0	
Landsat 8 TIRS/OLI	28 July 2019	11:20 (CST)	40 °C (max)	10	

Note: Considering that LST was not affected by COVID-19 in summer 2019 and that there are no suitable Landsat images for summer 2020, images in summer 2019 were used instead. Since Landsat 7 ETM+ image was damaged, striping was performed in ENVI 5.3 software through the striping repair plug-in.

There are three common LST inversion algorithms, including the atmospheric correction algorithm, split-window algorithm, and single-channel algorithm. Among them, the atmospheric correction algorithm is often used because of its simple calculation, easy parameter acquisition, and high inversion accuracy. Therefore, this method is applied to the LST inversion of Beilin District. The calculation is performed based on the study of Sobrino et al. [82]. Meanwhile, in order to reduce the influence of weather on the LST, the maximum and minimum method was used to normalize the LST of the three time periods [83], and the normalized land surface temperature (NDLST) of the study area was obtained (Figure 2).

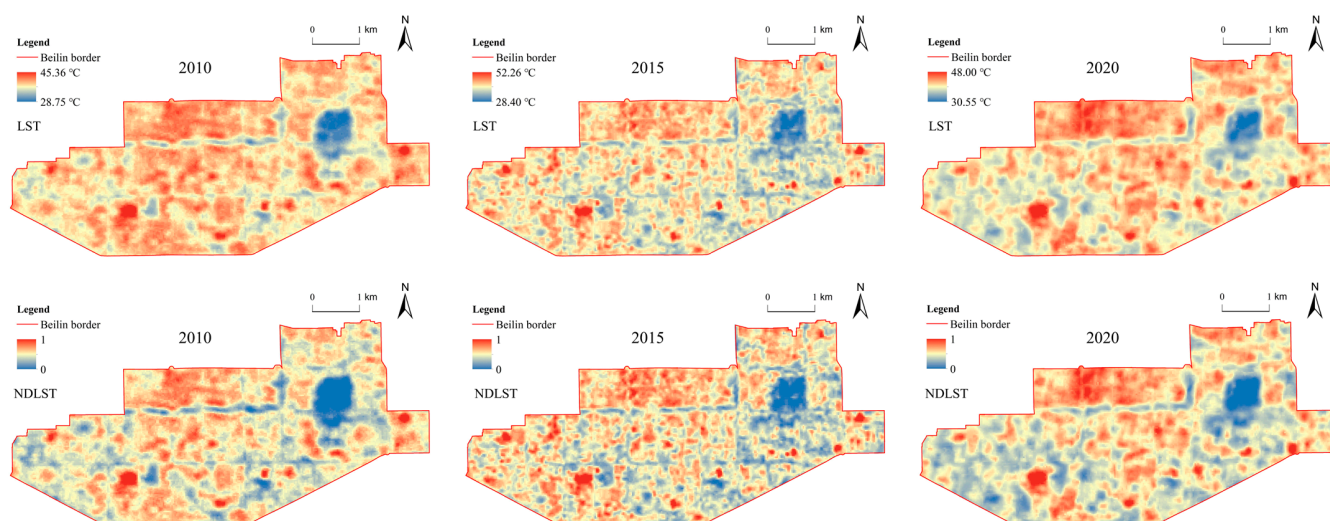


Figure 2. LST retrieval results and normalized LST in Beilin District.

2.2.2. Built Environment Dataset

UBE datasets mainly include Landsat images, land use, building footprint, road network, and impervious surface. In order to be consistent with the time of the LST, we collected the corresponding built environment data for 2010, 2015, and 2020 (Table 2). After comparing the building footprint (including height information) and Baidu street view (a free online panoramic map) in 2020, we found that there was a gap between the height information and the actual building height. Further manual sampling statistics also showed that the accuracy of the initial building height information was only around 64%. Therefore, building height corrections were then manually carried out via visual interpretation by comparing the height data with Baidu street view. According to manual sampling statistics, the accuracy of corrected data reached approximately 85%, which fulfils research requirements (Appendix A). At last, we used the height-corrected building footprint in 2020, combined with 1m resolution Google historical imagery, to invert the building footprint in 2010 and 2015.

Table 2. Data type and source of built environment dataset.

Data Type	Data Feature	Data Usage	Data Source
Landsat image	Raster data, 30 m × 30 m	Used to invert NDVI to calculate vegetation cover and invert surface albedo to classify LCZ.	USGS, https://earthexplorer.usgs.gov/ (20 January 2022)
Land cover	Raster data, 30 m × 30 m	Used to classify land use types in the LCZ classification process.	Global land cover dataset, https://www.resdc.cn/ (20 January 2022)
Building footprint	Vector data with height	Used to calculate the indicators of building height, building density, and building volume.	Amap, https://www.amap.com/ (20 January 2022)
Road network	Vector data with levels	Used to divide the boundaries of LCZ.	Amap, https://www.amap.com/ (20 January 2022)
Impervious surface	Raster data, 30 m × 30 m	Used to count the percentage of impervious surface.	Global impervious surface dataset, https://data.casearth.cn/ (20 January 2022)

2.3. Methods

2.3.1. Local Climate Zone Classification

WUDAPT method and GIS-based method are the two main LCZ classification methods. As an open source tool, WUDAPT method used spatial and spectral information of images as training samples to classify local climate zone based on remote sensing images and random forest classification. WUDAPT method has low data acquisition cost, but it has

high requirements on image quality and visual interpretation skills of researchers [84,85]. Based on multi-source UBE data, GIS-based classification method can classify local climate zone by accurately calculating LCZ indices, which is more suitable for high precision LCZ analysis in small areas [86]. Given the small area of Beilin District, GIS-based classification method based on ArcGIS 10.2 was applied to classify the LCZ of Beilin District in 2010, 2015, and 2020.

(1) Size classification and parameter selection. Existing literature mainly divides LCZ based on grid [48,57,87], which is convenient but tends to result in different parts of the same building being segregated into different LCZs and is not conducive to cooling design and management by city governments [88]. To overcome these shortcomings, the block and the road centerlines were used as the cell and the boundary of the LCZ, respectively. In total, 289 LCZ cells were found in Beilin District. The width of each cell of LCZ is 140–650 m, with an average of 260 m. Although the LCZ size of 100–150 m is a better compromise at the grid scale, a range of 200–500 m is more common at the block scale [84,89], making the division result relatively reasonable.

Stewart and Oke stated that LCZ could be divided from four dimensions: land cover, surface structure, construction materials, and anthropogenic heat emission [45]. However, due to the difficulty of data acquisition and geographical differences in specific cases, researchers will replace and choose more appropriate parameters in empirical study. For example, Yang et al. chose building height, building density, and land use [48]. Wu et al. used building height, building density, land use, pervious surface share, sky view factor, and street aspect ratio [87]. Geletič et al. selected building density, pervious surface share, impervious surface share, building/plant height, and the number of buildings [57]. As a typical old urban area, the proportion of pervious surface and impervious surface of Beilin District has not changed substantially in recent years. In addition, there is no good parameter to characterize anthropogenic heat emission. Therefore, building mean height (BH), building area ratio (BA), sky view factor (SVF), and surface albedo (SA) were used to classify LCZ types (Figure 3). The first three parameters can reflect the surface structure characteristics, and the last parameter can reflect the construction materials characteristics of Beilin District. The equations for BH, BA, and SVF are shown in Table 3, and the formula for SA is referred to by Liang et al. [90].

(2) LCZ classification criteria. We classify the LCZ based on the decision tree idea [51,91]. In addition, Beilin District is a typical urban center, and the land use is mainly for residential, commercial, office, and educational purposes. Some LCZ types proposed by Stewart and Oke are not found here, such as heavy industry zone (LCZ 10) [45], so it is necessary to make appropriate adjustments to Stewart and Oke's zoning criteria.

Step 1. Blocks with BA greater than 10% were defined as "built types", which means building zones, while those with BA less than 10% were defined as "land cover types", which means natural surface zones. On this basis, specific natural types of LCZ were determined in conjunction with land cover. Considering that there are fewer trees in Beilin District, woodland, shrub, and grassland are integrated into LCZ C.

Step 2. For the LCZ type of construction area, BH was used as the distinguishing parameter. Based on the architectural characteristics of Beilin District, blocks with BH larger than 30 m were classified as high-rise building zones, blocks with BH between 18 m and 30 m were defined as middle-level building zones, and blocks with BH between 3 m and 18 m were classified as low-rise building zones.

Step 3. On the basis of building height zones, BA, SVF, and SA were used to divide building density, which is the final LCZ type of building areas. Figure 4 shows the specific LCZ classification criteria. Compared with those in European and American countries, big cities in China have more dense buildings. Therefore, we further added six LCZ types including ultra-compact high-rise zone (LCZ 1A), ultra-compact mid-rise zone (LCZ 2A), ultra-compact low-rise zone (LCZ 3A), medium density low-rise zone (LCZ 3B), ultra-open high-rise zone (LCZ 4A), and ultra-open mid-rise zone (LCZ 5A).

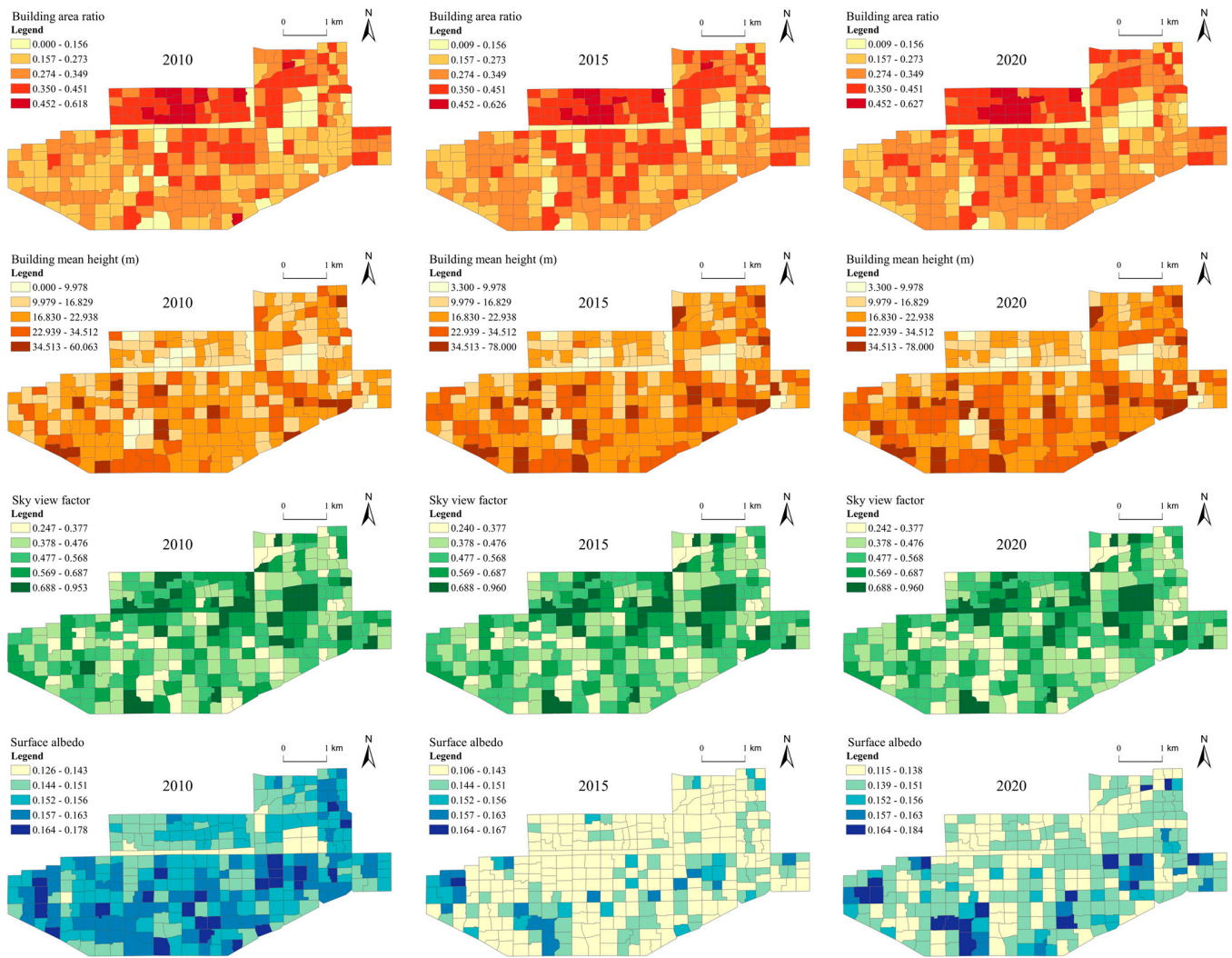


Figure 3. Parameters of LCZ classification in Beilin District.

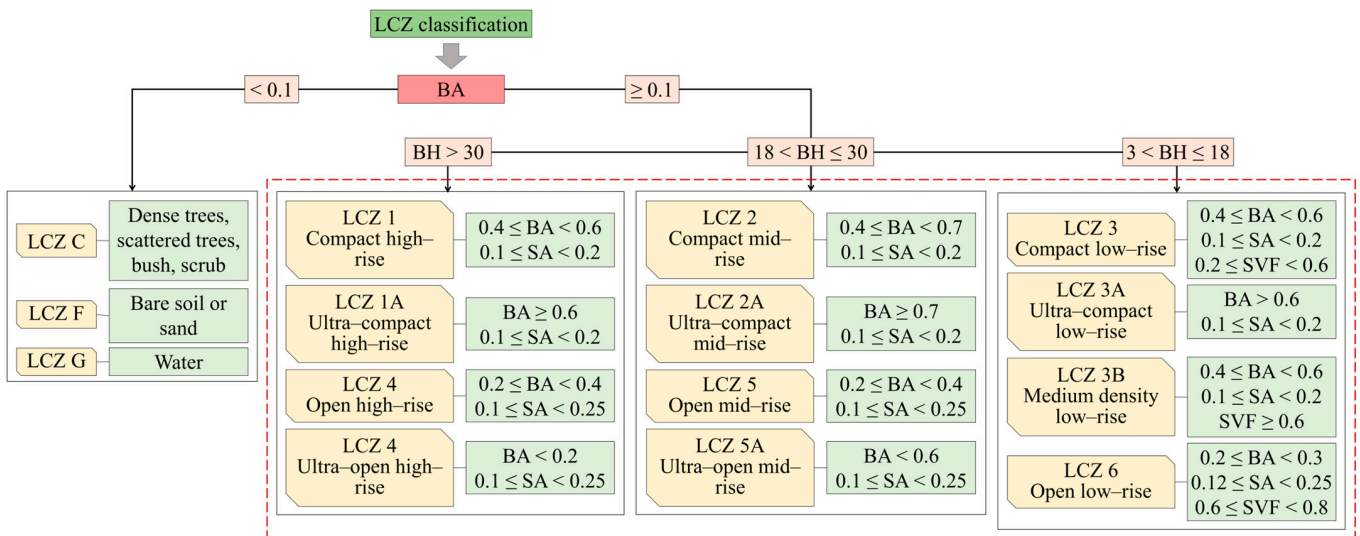


Figure 4. LCZ classification criteria of Beilin District.

2.3.2. Driving Indicators

Urban LST is influenced by a variety of factors, including land use, surface form, landscape pattern, human activities, meteorological conditions, and geographic location [92]. This paper mainly focuses on the influencing factors of LST from the perspective of the 2D and 3D forms of UBE. The 2D morphology could be represented by the underlying surface characteristics. Urban underlying surface adjusts the albedo and absorption rate of surface heat mainly through the proportion of blue, green, and gray infrastructure, thus affecting LST [93]. Referring to relevant studies [10,11,24,25], and considering that water body in Beilin District is very small, vegetation cover ratio (VC) and impervious surface area ratio (ISA) were used to represent urban underlying surface. The 3D morphology is represented by block building forms and plays a role based on height, area, openness, crowding, and construction intensity. It affects LST by altering the amount of solar radiation absorbed and stored by the city during the day, reducing the loss of long-wave radiation at night, reshaping the wind profile of urban canopies, lowering wind speeds, and reducing advection and turbulent heat dissipation [94]. According to the relevant studies [14–17,20,21,26–32,35–37], building mean height (BH), building area ratio (BA), building mean volume (BV), space congestion (SC), floor area ratio (FAR), and sky view factor (SVF) were used to represent block building form. Although BH, BA, and SVF are the parameters of LCZ classification, they are also important variables to characterize urban 3D morphology. The calculations of these indicators are shown in Table 3.

Table 3. Potential urban built environment indicators affecting LST.

Type	Indicator	Calculation Formula	Physical Meaning	Reference
Urban 2D morphology	Vegetation cover ratio (VC)	$VC = \frac{NDVI - NDVI_{min}}{NDVI_{max} - NDVI_{min}}$	Reflects the vegetation cover.	[95]
	Impervious surface area ratio (ISA)	$ISA = S/A$	Reflects the coverage of impervious surface.	[96]
Urban 3D morphology	Building mean height (BH)	$BH = \frac{1}{n} \times \sum_{i=1}^n H_i$	Reflects the overall height of buildings.	[17,29,35,36,97]
	Building area ratio (BA)	$BA = \frac{1}{A} \times \sum_{i=1}^n F_i \times 100\%$	Reflects the density of buildings.	[17,29,35,36,97]
	Building mean volume (BV)	$BV = \frac{1}{n} \times \sum_{i=1}^n (H_i \times F_i)$	Reflects the space occupied by buildings.	[29,35,85]
	Space congestion degree (SC)	$SC = \frac{1}{H_{max} \times A} \times \sum_{i=1}^n (H_i \times F_i)$	Reflects the congestion degree of buildings.	[35]
	Floor area ratio (FAR)	$FAR = \frac{1}{A} \times \sum_{i=1}^n (C_i \times F_i)$	Reflects the construction intensity of buildings.	[35]
	Sky view factor (SVF)	$SVF = 1 - \frac{1}{k} \times \sum_{i=1}^k \sin \gamma_i$	Reflects the sky openness.	[36,97,98]

Notes: VC are calculated by remote sensing inversion of NDVI. ISA is calculated directly from impervious surface data. BH, BA, BV, SC, FAR, and SVF are calculated by building footprint and height. The spatial resolution of NDVI, SVF are 30 m and 50 m, the average values of NDVI, SVF in each LCZ are calculated as the index values by zonal statistics. S is the area of impervious surface. A is the area of LCZ cell. NDVI, NDVI_{min}, and NDVI_{max} are the normalized vegetation index, the minimum value of normalized vegetation index, and the maximum value of normalized index, respectively. H_i, F_i, and C_i are the height, base area, and number of floors of building i, respectively. H_{max} is the maximum height of buildings in each LCZ. γ_i is the blocking angle of building height to azimuth, i, and k is the number of azimuths.

2.3.3. Geodetector

Geodetector, a set of statistical methods designed to analyze the spatial heterogeneity of geographic phenomena and to investigate the factors influencing the spatial heterogeneity, has no assumptions about the linearity of the variables. It is in the same category as analysis of variance (ANOVA), based on the assumption that “the spatial distributions of the independent and dependent variables should be similar if one of the independent variables has a significant effect on a dependent variable” [99]. The advantage of Geodetector is that it eliminates the linear effects between the independent variables, allowing it to detect both the contribution of a single independent variable to the dependent variable

and the contribution of two independent variables interacting with the dependent variable. We employed it to analyze the nonlinear role of UBE factors on the spatial differentiation of LST.

(1) Factor detection is used to calculate the extent to which a single built environmental factor influences the spatial differentiation of LST as follows:

$$q = 1 - \frac{1}{N\sigma^2} \sum_{h=1}^L N_h \sigma_h^2 \tag{1}$$

where q measures the driving force of a built environment factor on the spatial distribution of LST, N is the number of LCZ units, here 289, $h = 1, 2, 3, \dots, L$, and L is the number of partitions or strata, σ^2 is the total discrete variance of the LST of all LCZs, and σ_h^2 is the discrete variance of the surface temperatures of the LCZs in the h -th partition or stratum. Larger values of q indicate that the built environment factor is a stronger driver for LST and vice versa.

(2) Interaction detection is used to calculate the influence of two factor interactions on the spatial differentiation of LST. There are five interaction results: nonlinearly weakened, unilinearly weakened, bilinearly strengthened, nonlinearly strengthened, and mutually independent. Their mathematical explanations are given in Table 4.

Table 4. Interaction detection relationship.

Graphical Representation	Description	Interaction
	$q(X_i \cap X_j) < \min(q(X_i), q(X_j))$	Weaken, nonlinear
	$\min(q(X_i), q(X_j)) < q(X_i \cap X_j) < \max(q(X_i), q(X_j))$	Weaken, uni-
	$q(X_i \cap X_j) > \max(q(X_i), q(X_j))$	Enhance, bi-
	$q(X_i \cap X_j) > q(X_i) + q(X_j)$	Enhance, nonlinear
	$q(X_i \cap X_j) = q(X_i) + q(X_j)$	Independent

Legend: ● $\min(q(X_i), q(X_j))$; ● $\max(q(X_i), q(X_j))$; ● $q(X_i) + q(X_j)$; ▼ $q(X_i \cap X_j)$.

2.3.4. Geographically Weighted Regression

Since Geodetector was unable to distinguish between positive and negative effects of independent variables, this paper is supplemented with the geographically weighted regression model (GWR). As a locally weighted linear regression model, the GWR method adds the sample point location information into the regression parameters for properly analyzing the heterogeneity or non-stationarity characteristics of spatial data [100]. The core algorithm of GWR is still based on the least squares, with the difference lying in that GWR uses a weighting technique for local parameter estimation. We analyzed the local linear effect of UBE factors on the spatial differentiation of LST using the GWR method as follows:

$$y_i = a_0(u_i, v_i) + \sum_{j=1}^k b_j(u_i, v_i)x_{ij} + c_i \tag{2}$$

where y_i is the LST of the i -th LCZ unit, (u_i, v_i) is the spatial coordinate of the i -th LCZ unit, $a_0(u_i, v_i)$ is a constant term, $b_j(u_i, v_i)$ is the variable parameter of the j -th explanatory factor x_{ij} of the i -th LCZ unit, reflecting the spatial differentiation of the effect of different built environment factors on LST, and c_i is the random error term of the i -th LCZ unit, with $i = 1, 2, 3, \dots, 289$. The estimation of the variable parameter $b_j(u_i, v_i)$ in the above equation needs to be carried out by weighted least squares, which is the OLS model if $b_j(u_i, v_i)$ remains unchanged. GWR allows the evaluation of model fit by means of cross validation

(CV) or Akaike information criterion (AICc) in combination with an R^2 or adjusted R^2 . A smaller CV or AICc with a larger R^2 or adjusted R^2 results in higher model accuracy.

3. Results

3.1. LCZ Types

According to the classification, 15, 14, and 14 LCZ types were found in Beilin District in 2010, 2015 and 2020, respectively, with a total of 12 building zones and 3 natural surface zones (Figure 5). To verify the classification results, we compared the LCZ obtained by visual interpretation with the LCZ obtained by GIS classification and made a confusion matrix based on 50 randomly selected LCZ samples from satellite images and Baidu street view across the three years. The results showed that the overall accuracy of the classification was 0.80, 0.92, and 0.86, and the kappa coefficients were 0.75, 0.90, and 0.81 for 2010, 2015, and 2020, respectively, suggesting a good performance (Appendix B).

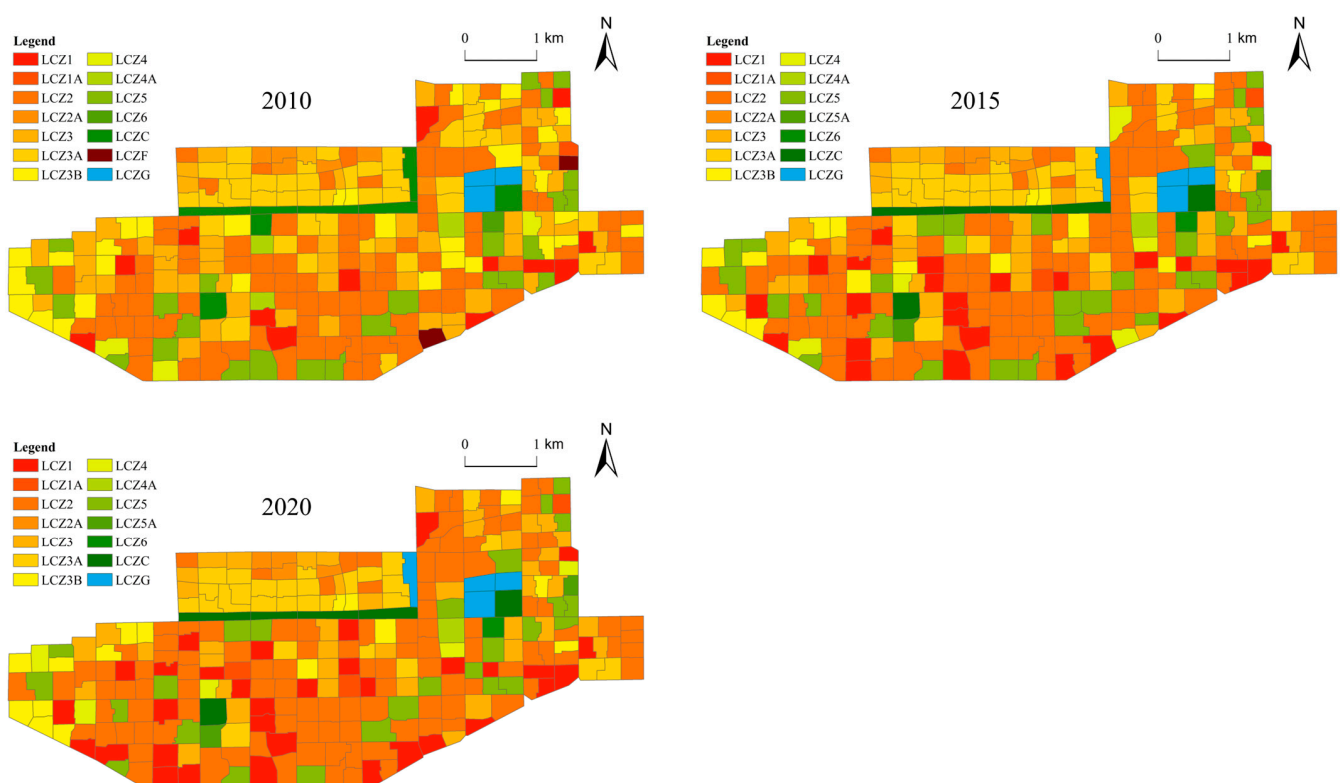


Figure 5. LCZ classification results in Beilin District.

Figure 6 shows the area proportions of different LCZ types in Beilin District in 2010, 2015, and 2020. Dense building zones in Beilin District account for a large share in area, while open building zones and natural surface zones account for a small share. In addition, from 2010 to 2020, the area of mid- and high-rise dense building zones continued to increase, while the area of low-rise dense building zones continued to decrease. The area ratio of LCZ 1, LCZ 2, and LCZ 5 increased from 4.55%, 34.63%, and 9.30% in 2010 to 12.05%, 40.69%, and 9.56% in 2020. The area ratio of LCZ 3, LCZ 3A, and LCZ 3B decreased from 16.14%, 14.10%, and 9.64% in 2010 to 12.89%, 8.97%, and 4.78% in 2020. The area of LCZ 1A, LCZ 2A, LCZ 4, LCZ 4A, LCZ 5A, LCZ 6, LCZ C, LCZ F, and LCZ G accounted for a small share, and they all varied by less than 1%.

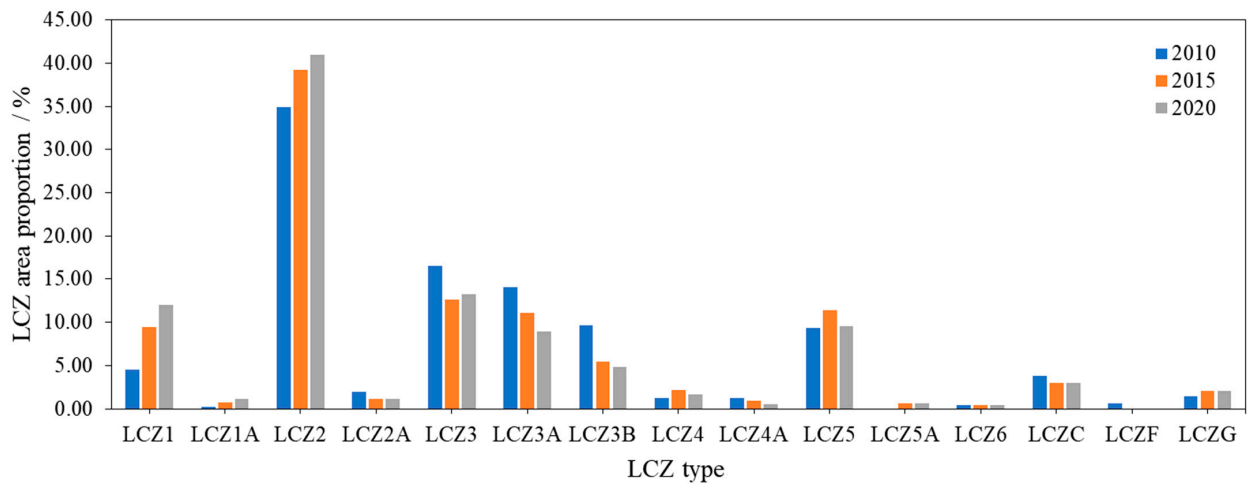


Figure 6. Area proportions of different LCZ types in Beilin District.

3.2. Spatio-Temporal Evolution Characteristics of LST

3.2.1. Temporal Variation of LST

Figure 7 shows the average values of NDLST of different LCZ types. The LST of different LCZ types is quite different in Beilin District. The LST of dense building zones is generally greater than that of open building zones and natural surface zones. From 2010 to 2020, the LST of mid- and low-rise dense building zones gradually increased, while that of high-rise open building zones gradually decreased. In 2010, the top three NDLSTs were LCZ 2A, LCZ 3A, and LCZ 1A, while the bottom three were LCZ G, LCZ 6, and LCZ C. In 2015, the top three NDLSTs were LCZ 2A, LCZ 3A, and LCZ 3B, while the bottom three were LCZ G, LCZ 6, and LCZ C. In 2020, the top three NDLSTs were LCZ 2A, LCZ 3A, and LCZ 3, while the bottom three were LCZ G, LCZ 6, and LCZ 4A. From 2010 to 2020, NDLST in LCZ 2A, LCZ 3, LCZ 3A, LCZ 6, and LCZ G increased noticeably, while NDLST in LCZ 1A, LCZ 4, and LCZ 4A decreased noticeably. The NDLST in LCZ 1, LCZ 2, LCZ 3B, LCZ 5, and LCZ C showed little change.

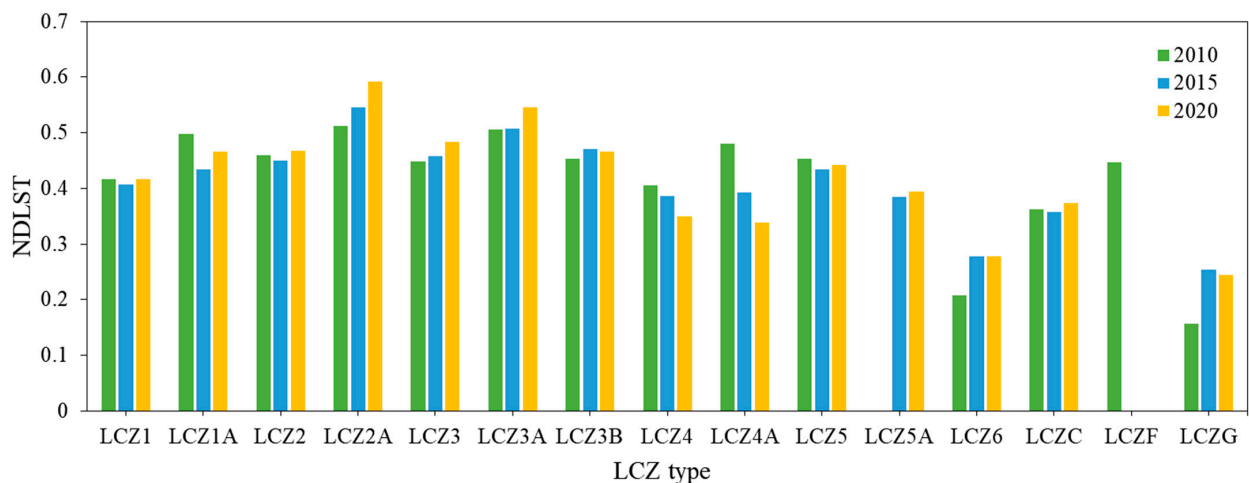


Figure 7. Average values of NDLST of different LCZ types in Beilin District.

Notably, the LST of the low-rise open building zone (LCZ 6) is relatively low, even lower than that of the vegetation (LCZ C). One possible reason is that the three open low-rise building areas are affected by the cold island effect of the adjacent Xingqing Park.

3.2.2. Spatial Changing Characteristics of LST

Figure 8 shows the changing characteristics of the LST in Beilin District. We took the difference of NDLST between different years and distinguished the temperature variation of different LCZs as increasing, decreasing, and non-significant zones using one standard deviation of 2010–2015 as the threshold. The area with increased LST was smaller than that with decreased LST from 2010 to 2015, while the opposite was true from 2015 to 2020. On the whole, the regions with increased LST were obviously more than those with decreased LST. From 2010 to 2015, the proportion of areas with increased LST was 10.73%, and the proportion of areas with decreased LST was 16.26%. From 2015 to 2020, the proportion of areas with increased LST was 23.53%, and the proportion of areas with decreased LST was 11.76%. From 2010 to 2020, the proportion of areas with increased LST was 20.76%, and the proportion of areas with decreased LST was 13.84%. Overall, the regions with increased LST were concentrated in the center and northeast, while those with decreased LST were in the southwest.

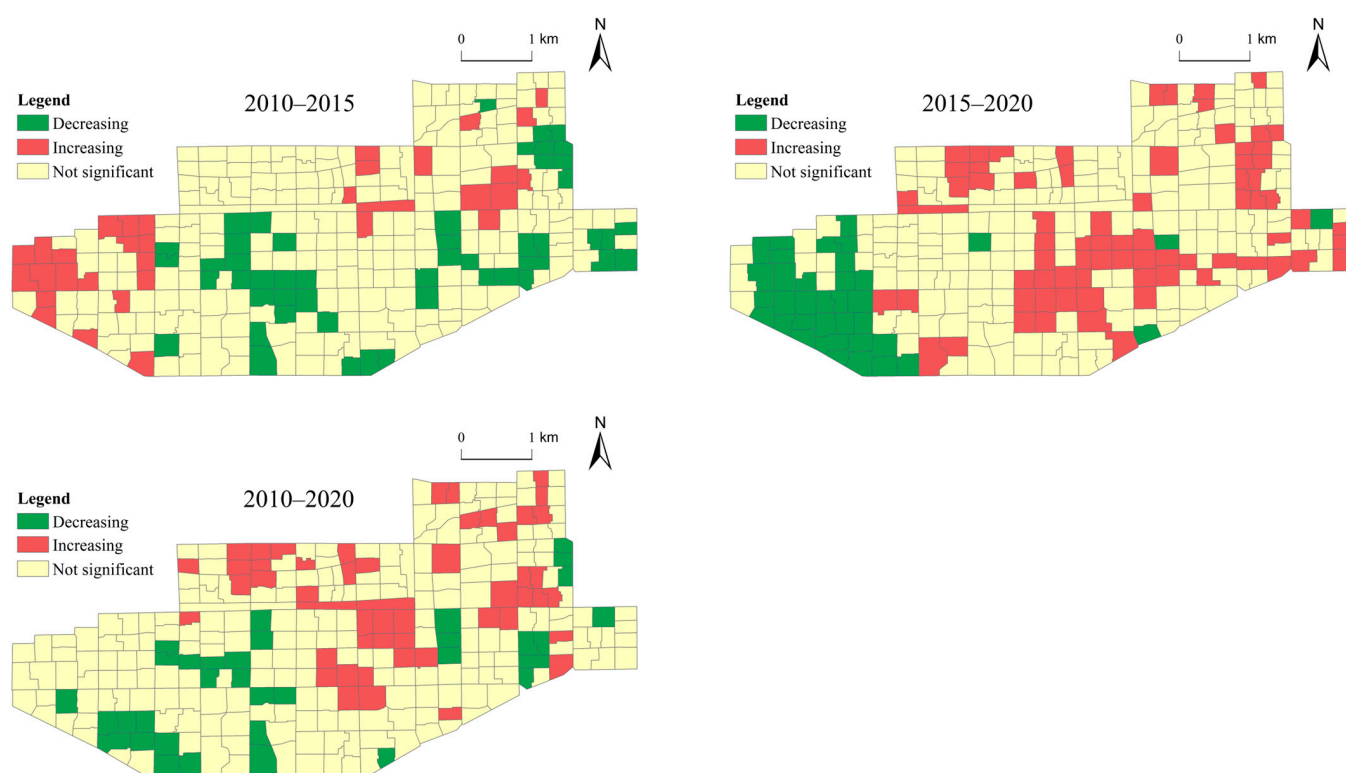


Figure 8. Spatial changing patterns of NDLST in Beilin District.

3.3. Influence Effect Based on Geodetector

3.3.1. Factor Detection

We used Excel as the platform to run the factor detection model with the NDLST as the dependent variable, and VC, ISA, BH, BA, BV, SC, SVF, and FAR as the independent variables. Table 5 shows the results of factor detection of the LST in different LCZs in Beilin District. The effects of UBE factors on LST show large differences, and the force of 2D indicators is larger than that of 3D indicators, with 2D indicators decreasing in general, BA and SC in 3D indicators increasing, FAR staying relatively stable, and BH changing from insignificant to significant in their force. In 2010, VC, ISA, BA, SC, and FAR all passed the significance test of 0.05, and the average action strength was 0.23. The ISA had the largest value of 0.46, and FAR had the smallest value of 0.08. In 2015, VC, ISA, BA, SC, and FAR all passed the significance test of 0.1, and the average action strength was 0.20. ISA had the largest value of 0.31, and FAR had the smallest value of 0.05. In 2020, VC, ISA, BH, BA, SC,

and FAR all passed the significance test of 0.01, and the average action strength was 0.17. BA had the largest value of 0.30, and FAR had the smallest value of 0.07.

Table 5. Factor detection result.

Period	Value	VC	ISA	BH	BA	BV	SC	SVF	FAR
2010	q-value	0.36 ***	0.46 ***	0.01	0.16 ***	0.00	0.09 **	0.01	0.08 ***
	p-value	0.00	0.00	0.98	0.00	1.00	0.03	0.68	0.00
2015	q-value	0.24 ***	0.31 ***	0.09	0.22 ***	0.05	0.15 **	0.00	0.05 *
	p-value	0.00	0.00	0.38	0.00	0.80	0.01	1.00	0.07
2020	q-value	0.20 ***	0.20 ***	0.11 ***	0.30 ***	0.04	0.17 ***	0.00	0.07 ***
	p-value	0.00	0.00	0.00	0.00	0.87	0.00	0.96	0.00

Note: *** presents $p < 0.01$, ** presents $p < 0.05$, * presents $p < 0.10$.

Between 2010 and 2020, the effects of VC and ISA gradually decreased, with the ISA experiencing the largest decrease at 0.26, while BA and SC saw their effects increasing, with BA experiencing the largest increase at 0.14. The effects of FAR were relatively stable, decreasing only by 0.01. In addition, the effect of BH gradually changed from insignificant to significant, while the effects of BV and SVF remained insignificant.

3.3.2. Interaction Detection

We used Excel as the platform to run the interaction detection model with the NDLST as the dependent variable, and VC, ISA, BH, BA, SC, and FAR as the independent variables. BV and SVF failed the significance test in all three years and therefore were excluded in the analysis. Figure 9 shows the results of interaction detection. The interaction of the UBE with LST mainly showed an enhancement effect. The interaction effect of 2D indicators was larger than that of 3D indicators. Compared to the gradual decrease in 2D indicators, the interaction effect of BH, BA, and SC in 3D indicators increased, and that of FAR remained relatively stable. In 2010, the mean values of the interactions of VC, ISA, BH, BA, SC, and FAR were 0.46, 0.55, 0.26, 0.32, 0.28, and 0.27, with VC, ISA, and BA having the strongest interactions. In 2015, the mean values of the six factor interactions were 0.37, 0.39, 0.29, 0.34, 0.30, and 0.27, with VC, ISA, and BA still having the strongest interactions. In 2020, the mean values of the six factor interactions were 0.35, 0.34, 0.30, 0.38, 0.31, and 0.27, with VC, ISA, and BA continuing to have the strongest interactions. Between 2010 and 2020, the mean interaction of VC and ISA gradually decreased by 0.11–0.18, while the mean interaction of BH, BA, and SC gradually increased by 0.03–0.05, and the mean interaction of FAR remained relatively stable with a small change.

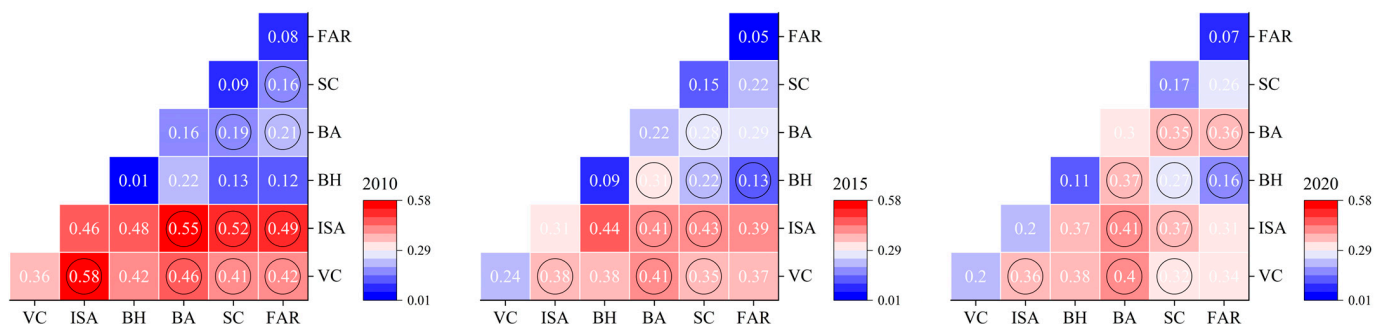


Figure 9. Interaction detection results. Circles indicate bilinear enhancement, no circle indicates non-linear enhancement.

3.4. Influence Effect Based on GWR

We ran the GWR model using GWR 4.0 as the platform with NDLST as the dependent variable and VC, ISA, BH, BA, SC, and FAR as the independent variables. BV and SVF had

no significant effects in any of the three years above, and they were not included in the model (Appendix C).

Table 6 shows the statistical parameters of the local regression coefficients, and Table 7 shows the statistical results of the direction of action of the local regression coefficients. (a) VC and FAR mainly acted negatively, with the mean of VC changing from -0.27 to -0.15 and that of FAR from -0.20 to -0.16 , indicating that the strength of negative actions of VC and FAR was decreasing. (b) ISA, BA, and SC mainly acted positively, with the mean of ISA changing from 0.12 to 0.20 , that of BA from 0.12 to 0.19 , and that of SC from 0.04 to 0.04 , indicating that ISA and BA were increasing their strength of positive action, and SC had a relatively stable strength. (c) BH acted both positively and negatively. That is, it promoted an LST increase and decrease at the same time, with the proportion of positive and negative effect areas changing from 68% and 31% to 0% and 100% , and the mean of BH changing from 0.05 to -0.04 , indicating that the effect of BH on the LST gradually shifted from positive to negative.

Table 6. Statistics of regression coefficients of GWR model.

Period	Type	VC	ISA	BH	BA	SC	FAR
2010	Min	-0.49	-0.17	-0.16	-0.07	-0.06	-0.41
	Max	-0.18	0.33	0.21	0.31	0.27	0.03
	Mean	-0.27	0.12	0.05	0.12	0.04	-0.20
	Median	-0.27	0.12	0.03	0.12	0.04	-0.20
	St. dev.	0.06	0.08	0.08	0.08	0.06	0.10
2015	Min	-0.22	0.08	-0.05	0.11	0.01	-0.25
	Max	-0.08	0.29	0.06	0.22	0.06	-0.12
	Mean	-0.16	0.19	0.02	0.15	0.04	-0.19
	Median	-0.18	0.18	0.02	0.15	0.04	-0.19
	St. dev.	0.04	0.04	0.03	0.03	0.01	0.04
2020	Min	-0.19	0.08	-0.06	0.16	0.03	-0.19
	Max	-0.12	0.27	-0.02	0.21	0.07	-0.12
	Mean	-0.15	0.20	-0.04	0.19	0.04	-0.16
	Median	-0.15	0.22	-0.04	0.19	0.04	-0.15
	St. dev.	0.02	0.06	0.01	0.01	0.02	0.02

Note: The adjusted R^2 of the OLS model was 0.71 , 0.68 , and 0.66 , while the corresponding AICc was -1078 , -1089 , and -991 in 2010, 2015, and 2020, respectively. In contrast, the GWR model had adjusted R^2 of 0.79 , 0.76 , and 0.68 and corresponding AICc of -1110 , -1163 , and -1000 . The GWR model displayed a larger adjusted R^2 and smaller AICc, indicating that the GWR model is more appropriate.

Table 7. Statistics of influence effect direction of GWR model.

Period	Direction	VC	ISA	BH	BA	SC	FAR
2010	Positive	0%	91%	68%	92%	80%	2%
	Negative	100%	8%	31%	7%	20%	98%
2015	Positive	0%	100%	64%	100%	100%	0%
	Negative	100%	0%	36%	0%	0%	100%
2020	Positive	0%	100%	0%	100%	100%	0%
	Negative	100%	0%	100%	0%	0%	100%

4. Discussion

4.1. Spatial Differentiation of LST in Different LCZs

This paper found that LST exhibited obvious spatial heterogeneity across different LCZs. The highest LST is found in dense building zones (LCZ 1-LCZ 3A), followed by open building zones, vegetation, and bare ground (LCZ 4-LCZ 5A, LCZ C, and LCZF), and the lowest LST is found in low-rise open building zones and waters (LCZ 6 and LCZ G). The LST is higher in dense building zones due to more hardened surfaces and thus more heat

absorption and poor ventilation [62]. The LST is lower in open building zones and natural surface zones due to fewer hardened surfaces and thus less heat absorption, coupled with good air circulation, and transpiration from vegetation and waters [57]. However, the LST in the high-rise building zones (LCZ 1, LCZ 1A, LCZ 4, and LCZ 4A) is slightly lower than that in the mid-rise building zones (LCZ 2, LCZ 2A, LCZ 5, and LCZ 5A) due to the cooling effect from building shadows [101], agreeing with the findings of most studies [52–54,56]. We also found that the rise in the overall LST within Beilin District was mainly driven by an obvious increase in the area proportion of mid- and high-rise dense building zones with higher LSTs (LCZ 1, LCZ 1A, and LCZ 2) over the study period.

In addition, it is observed that the LST does not increase uniformly in all local climate zones during urban warming. In low- and mid-rise dense building areas (LCZ 2A, LCZ 3, and LCZ 3A), the increase in LST is more noticeable, while in high-rise open building zones (LCZ 4 and LCZ 4A), the decrease in LST is more noticeable. This phenomenon has also been observed in studies on urban agglomerations and individual cities [46,47,63,102]. One possible explanation is that during the urban construction and renovation process in Beilin District, the whole region is further extended to two and three dimensions, and the overall heat island effect is further enhanced. However, the high-rise open building zones have certain places that can increase green space, which helps to mitigate the heat island intensity, while the low- and mid-rise dense building zones cannot accommodate more green space due to space constraints, leading to an increase in the LST.

4.2. Impact Effect of Built Environment on LST

We found that there are large differences in the intensity and direction of the effects of 2D and 3D built environment indicators on the LST, as well as in the changing trend. The overall influence of 2D indicators is relatively larger than that of 3D indicators, which is also a common phenomenon in existing studies [15,16,40]. It suggests that the force of 2D indicators on the LST by regulating the physical environment of the ground surface is stronger than that of 3D indicators by regulating the combination of building forms [92,94].

In terms of 2D indicators, VC and ISA showed significant effects on the LST, with VC stably acting negatively and ISA stably acting positively. Established studies have shown that VC has both shading and transpiration effects [103], while ISA changes thermal characteristics such as surface thermal conductivity and specific heat capacity [104]. It has been widely confirmed that the two have promoting and alleviating effects on the LST, respectively [11,12,62,105–108]. We also found that the strength of the action of VC and ISA on the LST decreased gradually with the increase in vegetation cover and proportion of impervious surface area (Figure 10). A few studies also detected that the correlation coefficients between the NDVI and LST of the built-up areas of the city became smaller year by year [106]. One possible reason is that the city produced a large amount of anthropogenic heat when performing 3D expansion, and that the 3D indicators' increasing ability of absorbing heat and shading on the LST impaired the correspondence between the 2D indicators and the LST.

In terms of 3D indicators, BA and SC showed relatively stable positive effects, FAR showed relatively stable negative effects, while BH was changing from insignificant to significant, from a positive role to a negative role in action. A larger BA is more likely to result in absorption of solar radiation and less likely to dissipate heat, thus contributing to a rise in the LST [31,36]. A larger BH results in a larger area of the building and ground directly exposed to direct sunlight, normally leading to high temperatures [36], while producing more shading and ventilation [109]. FAR is a comprehensive indicator that integrates building density and building height, with ability to absorb heat and provide shade [110]. A larger SC can accommodate more human activity and thus generate more anthropogenic heat [28], but it also provides more shaded space [35]. Established studies have found a greater warming effect of BA [15–17,29,36,41,97] and a greater cooling effect of BH [15–17,29,36,97] on the LST, and a few studies have also found the cooling effect of FAR [28,35], as well as the warming effect of SC [28] on the LST. Our conclusions are

in general agreement with them, except the observation of some positive effects of BH. This paper also found that the force of BA on the LST increased with a larger building density, the force of FAR decreased slightly with an increasing floor area ratio, the force of BH increased with increasing building height, and the force of SC also increased with a slight increase in spatial crowding. Changes in BA, FAR, and SC should be attributed to the gradual increase in thermal radiation and anthropogenic heat affecting the force of these indicators on LST, and changes in BH should be attributed to its threshold and only in the range of the threshold value can it play a significant role in thermal regulation. In addition, we found that the effects of BV and SVF on the LST were not significant in the three years. The mechanism of action of BV and SVF on LST is similar to that of SC and BH, respectively, and is also modulated by anthropogenic heat and shade effects [17,111], as well as direct sunlight and shade effects [112]. Established studies have detected positive [29,36,62,113,114], negative [17,31,97,112], and insignificant [15,62,115] effects of BV and SVF on LST, which should be closely related to the research methodology and case-site characteristics of different research protocols.

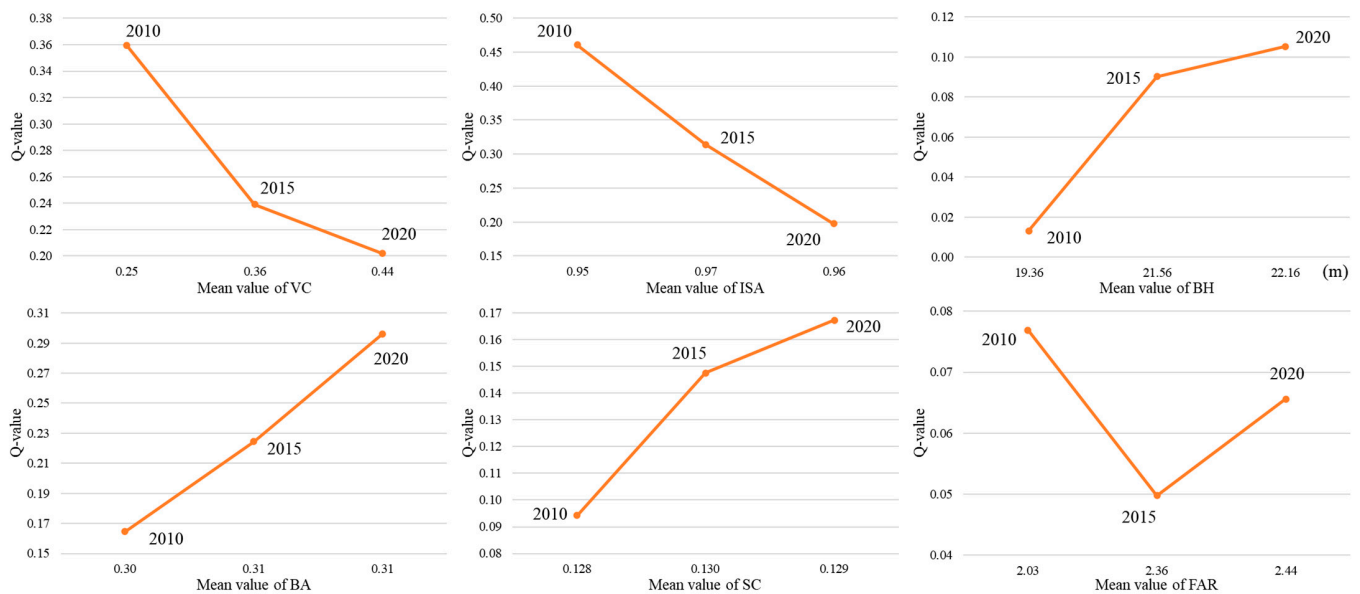


Figure 10. Relationship between the mean value of UBE indicators and their impact on LST. Horizontal axis is the average value of the independent variables, and vertical axis is the factor detection value of the Geodetector.

In addition, it was found that despite the different directions of action, the interaction between different indicators still showed an enhancement effect. The finding was also observed in a few studies [116], suggesting that LST was affected by the combined effects of the superimposed UBE indicators. It was also found that the interaction effect of 2D indicators in three years was relatively larger than that of 3D indicators. However, the interaction of the 2D indicators decreased, the interactions of BH, BA, and SC in the 3D indicators increased (with BA having the strongest interaction), and the interaction of FAR remained relatively stable, suggesting that the strength of the interaction is closely related to the force of the indicator itself. The takeaway from this is that optimizing the LST by tuning VC, ISA, and BA works well because of the possibility to simultaneously modulate direct and interactive effects of all the three.

4.3. Optimal Solution of Impact Effect on LST

Some statistical bias in the local regression parameters estimated by GWR makes it essential to analyze the built environment indicators together with their influencing effects and the NDLST to explore the optimal solution of the UBE indicators regulating the LST. This paper found that the overall R^2 of the quadratic polynomial regression equation was slightly larger than that of the primary polynomial regression equation, indicating that the influence of the UBE on the LST presents a parabolic or inverted parabolic shape. That is, there is an inflection point that can regulate the LST to a great extent. However, the inflection point values of different indicators vary considerably, and even the inflection point values of the same indicator vary somewhat from year to year. The inflection points for VC in the three years were roughly 0.3, 0.4, and 0.4, and values greater than them would give better cooling results. The inflection point of BH in all three years fell roughly in the range of 15–20 m, where a better cooling result can be obtained. The inflection point of SC in the three years fell roughly at 0.15, and values below that allow better control over the warming effect. The inflection point of FAR in the three years fell roughly between 2 and 3, a range allowing a better cooling result. The ISA and BA had no observable inflection points (Figure 11). Established studies have shown inflection points in the effects of BH, VC, and FAR on the LST [44,117–119], and some studies have also found inflection points in the ISA and BA [118–120]. This paper is in general agreement with these conclusions, except for differences in the inflection point values and whether there is an inflection point in the ISA and BA. The difference should be related to the case site selected and the method of calculation.

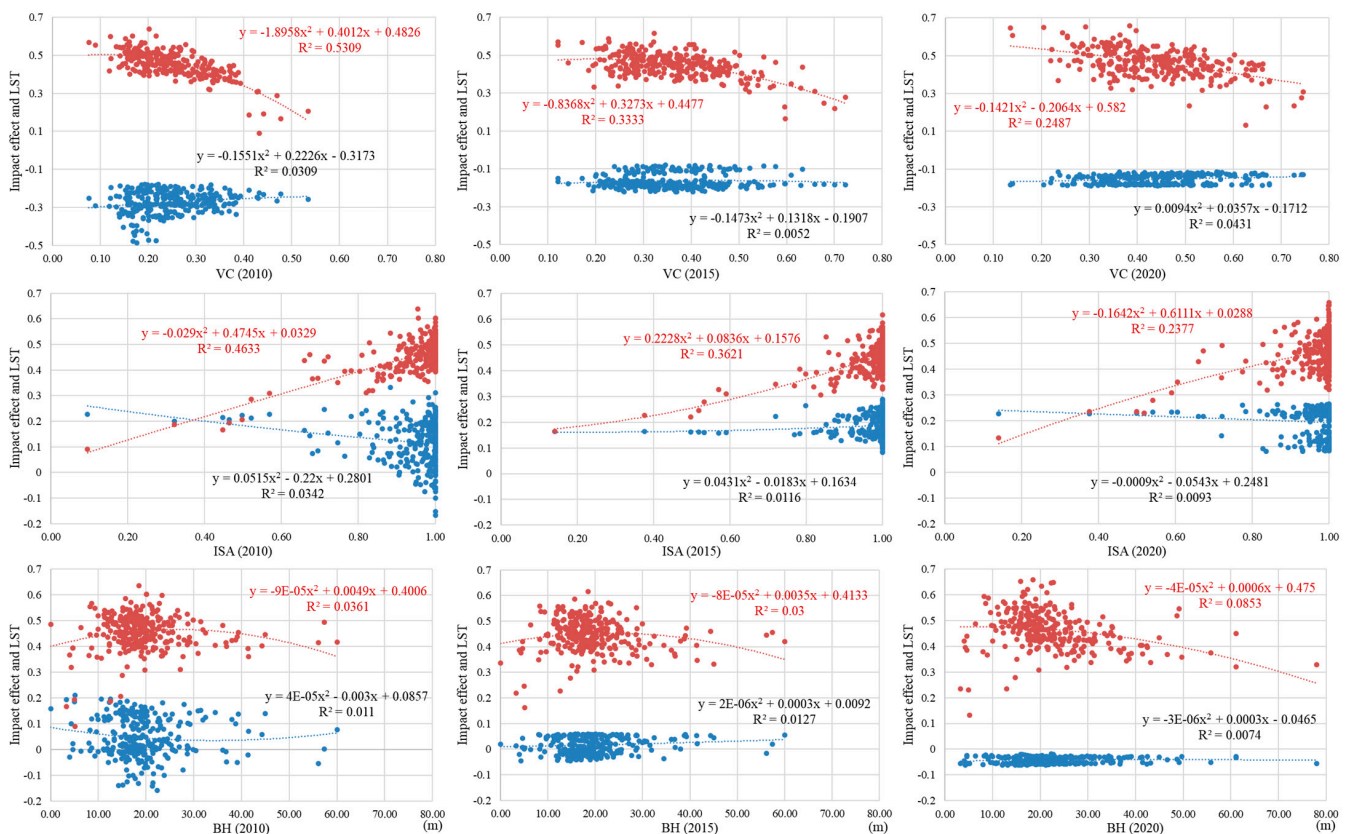


Figure 11. Cont.

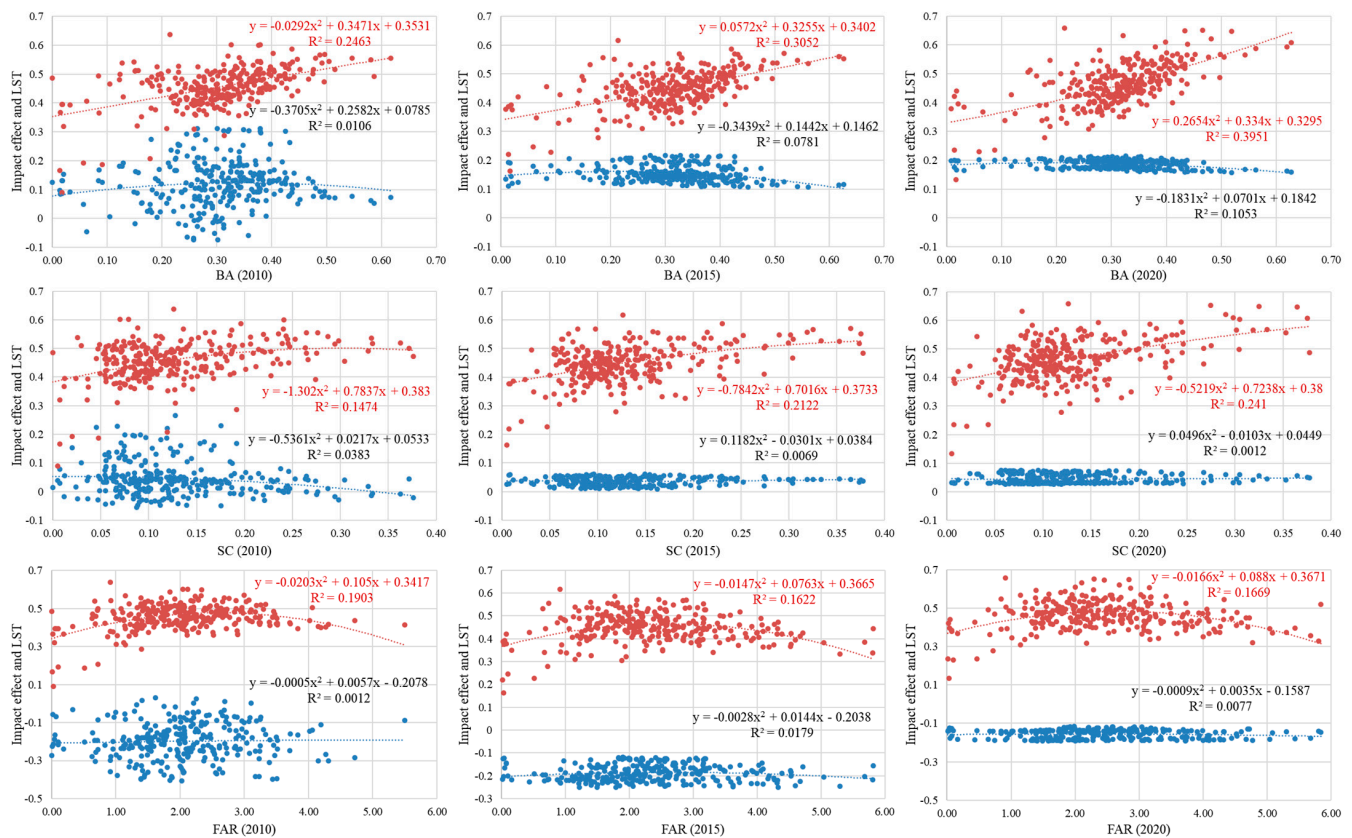


Figure 11. Relationships between UBE indicators and their impact effects and the LST. Horizontal axis is the independent variable value of different LCZs, red scatter points are the LST value, and blue scatter points are the influence effect value of GWR.

4.4. Insights and Shortcomings

The integration of thermal principles into urban planning and management can be an effective solution to urban warming. The novelty of this research lies in the combination of LCZ theory and spatial heterogeneity regression method to explore the dynamic influence of the UBE on the LST. This unique combination allows for a more accurate depiction of the variations in the LST across different LCZs over time, as well as the direct and interactive effects of different UBE indicators on the LST, and to further analyze in depth the local change rules of the influencing effects. The findings of this paper provide better insights for the regulation of the thermal environment in urban built-up areas: (1) The influence of 2D space on the LST is stronger than that of 3D space, and the optimization of 2D space should be focused on, such as increasing vegetation and softening the ground. But with further 3D expansion of the urban space, the focus should be placed on the optimization of 3D space, such as increasing the open space and the shaded sheltering surface in the construction. VC, ISA, and BA are the most critical morphological indicators, and their direct and interaction effects on LST regulation should be maximized. (2) The lean and open tower complex with a low density, high floors, and large spacing is the optimal cooling building combination, which can effectively play the role of building form in regulating the LST. VC, BH, SC, and FAR have obvious thresholds for their influence on the LST. Designing the built environment against this threshold interval maximizes the role of the UBE in regulating the LST, but attention should be paid to how this threshold changes at different stages of urban development.

There are also some limitations. (1) The study area is small in size, mainly restricted by the difficulty of data collection and collation, which leads to a small number of LCZ samples and thus may bring some statistical deviations. (2) This paper only discussed the spatial heterogeneity relationship between the UBE and LST in Xi'an, so the universality

of the conclusion still needs to be further verified. (3) This paper found that a number of UBE indicators had evident thresholds for their influence on the LST. But given the space constraints, the discussion of the threshold effect is not deep enough and needs to be further studied.

5. Conclusions

This paper explored the multidimensional dynamic impacts of the urban 2D and 3D built environments on the LST during the period of 2010–2020 based on a case study of Beilin District of Xi'an, a typical high-temperature area with obvious differences in the built environment. The study was conducted by a combined use of multi-source geographic data, GIS tools, remote sensing inversion, and regression analysis, based on the LCZ framework from the perspective of spatial-temporal heterogeneity. The conclusions are as follows:

- (1) In Beilin District, 15, 14, and 14 LCZ types were found in the years 2010, 2015, and 2020, respectively. Dense building zones in Beilin District account for a large share in the area, while open building zones and natural surface zones account for a small share. From 2010 to 2020, the area of mid- and high-rise dense building zones continues to increase, while the area of low-rise dense building zones continues to decrease.
- (2) The LST of different LCZ types in Beilin District is markedly different. The LST of dense building zones is generally higher than that of open building zones and natural surface zones. The LST of mid- and low-rise dense building zones increased gradually, while the LST of high-rise open building zones decreased gradually. The warming area of Beilin District is obviously more than the cooling area.
- (3) The 2D built environment indicators had a larger force on the LST than 3D indicators. The force of VC decreased from 0.36 to 0.20 and ISA from 0.46 to 0.20; the force of BA increased from 0.16 to 0.30 and SC from 0.09 to 0.17; the force of FAR was relatively stable at 0.07–0.08; and the force of BH changed from insignificant to significant. The interaction of the built environment on the LST showed an enhancement effect, which was greater for 2D than for 3D indicators. The force of VC and ISA gradually decreased, while the force of BH, BA, and SC gradually increased, and FAR was relatively stable.
- (4) VC and FAR showed negative effects, with the average action intensity of VC decreasing from -0.27 to -0.15 , FAR from -0.20 to -0.16 . ISA, BA, and SC showed positive effects, with the average action intensity of ISA increasing from 0.12 to 0.20 and BA from 0.12 to 0.19. SC remained stable at 0.04. BH gradually acted from positively to negatively, with the average action intensity changing from 0.05 to -0.04 .

Author Contributions: Conceptualization, K.Z. and X.H.; methodology, M.Q., X.Y. and L.L.; software, M.Q., X.Y. and L.L.; validation, M.Q., X.Y. and L.L.; formal analysis, K.Z.; investigation, M.Q., X.Y. and L.L.; resources, M.Q., X.Y. and L.L.; data curation, M.Q., X.Y. and L.L.; writing—original draft preparation, K.Z.; writing—review and editing, K.Z.; visualization, K.Z.; supervision, X.H.; project administration, X.H.; funding acquisition, X.H. All authors have read and agreed to the published version of the manuscript.

Funding: The research is funded by the National Natural Science Foundation of China (No. 41971178).

Data Availability Statement: The data presented in this study are available in article. All data were obtained from open-source websites, and the websites are marked at the corresponding data positions in the text. The data were collected between February and October 2022.

Conflicts of Interest: The authors declare no conflict of interest.

Appendix A

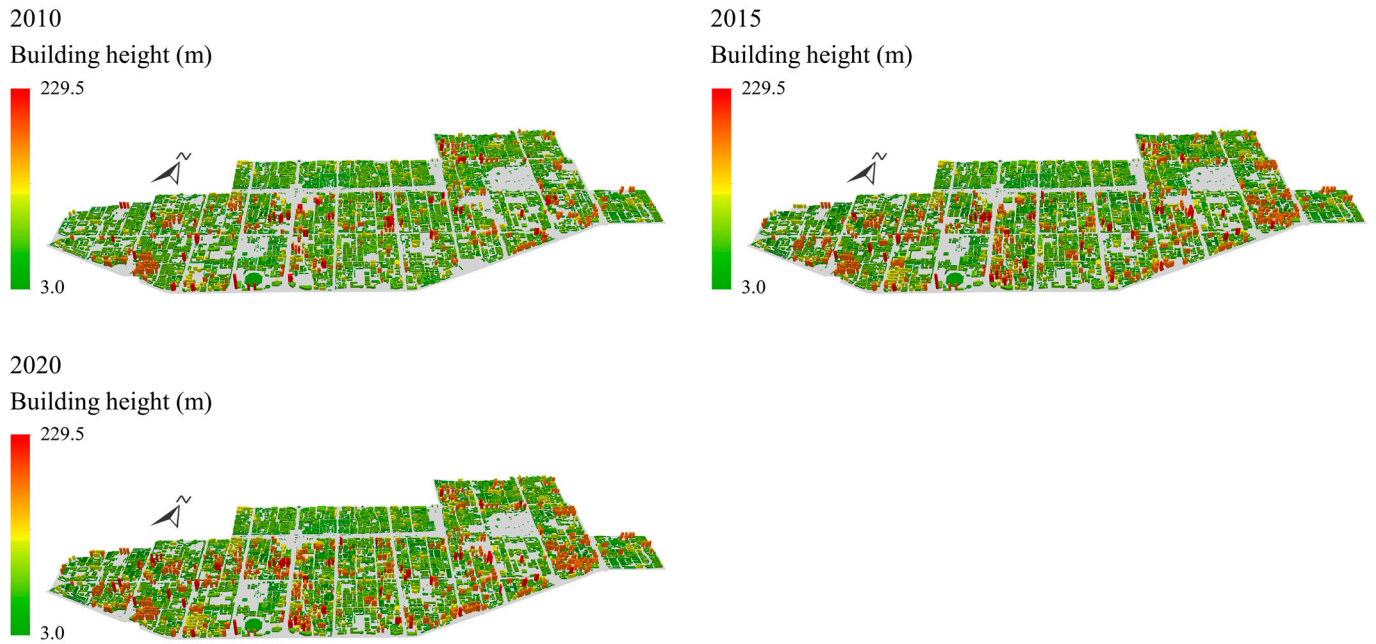


Figure A1. The 3D building morphology in Beilin District.

Appendix B

Table A1. Confusion matrix of LCZ in 2010 (overall accuracy is 0.80, kappa coefficient is 0.75). Horizontal columns are the results of visual interpretation and vertical columns are the results of GIS classification.

Visual \ GIS	LCZ 1	LCZ 1A	LCZ 2	LCZ 3	LCZ 3A	LCZ 3B	LCZ 4	LCZ 4A	LCZ 5	LCZ C	LCZ G	Total Zone	Mapping Accuracy (%)
LCZ 1	1	0	0	0	0	0	0	0	0	0	0	1	100
LCZ 1A	1	0	0	0	0	0	0	0	0	0	0	1	0
LCZ 2	0	0	13	2	0	0	0	0	0	0	0	15	86.7
LCZ 3	0	0	1	7	1	0	0	0	1	0	0	10	70
LCZ 3A	0	0	0	0	6	0	0	0	0	0	0	6	100
LCZ 3B	0	0	0	0	0	5	0	0	0	0	0	5	100
LCZ 4	0	0	0	0	0	0	0	1	0	0	0	1	0
LCZ 4A	0	0	0	0	0	0	0	0	1	0	0	1	0
LCZ 5	0	0	0	1	0	1	0	0	6	0	0	8	75
LCZ C	0	0	0	0	0	0	0	0	0	1	0	1	100
LCZ G	0	0	0	0	0	0	0	0	0	0	1	1	100
Total Zone	2	0	14	10	7	6	0	1	8	1	1	50	
Mapping accuracy (%)	50	0	93	70	86	83	0	0	75	100	100		

Table A2. Confusion matrix of LCZ in 2015 (overall accuracy is 0.92, kappa coefficient is 0.90).

Visual GIS	LCZ 1	LCZ 1A	LCZ 2	LCZ 2A	LCZ 3	LCZ 3A	LCZ 3B	LCZ 4A	LCZ 5	LCZ C	LCZ G	Total Zone	Mapping Accuracy (%)
LCZ 1	7	0	0	0	0	0	0	0	0	0	0	7	100
LCZ 1A	1	0	0	0	0	0	0	0	0	0	0	1	0
LCZ 2	0	0	16	0	0	0	0	0	0	0	0	16	100
LCZ 2A	0	0	0	1	0	0	0	0	0	0	0	1	100
LCZ 3	0	0	0	0	4	0	0	0	0	0	0	4	100
LCZ 3A	0	0	0	0	0	8	0	0	0	0	0	8	100
LCZ 3B	0	0	0	0	1	0	2	0	0	0	0	3	67
LCZ 4A	0	0	0	0	0	1	0	1	0	0	0	2	50
LCZ 5	0	0	0	0	0	0	1	0	5	0	0	6	83
LCZ C	0	0	0	0	0	0	0	0	0	1	0	1	100
LCZ G	0	0	0	0	0	0	0	0	0	0	1	1	100
Total Zone	8	0	16	1	5	9	3	1	5	1	1	50	
Mapping accuracy (%)	88	0	100	100	80	89	67	100	100	100	100		

Table A3. Confusion matrix of LCZ in 2020 (overall accuracy is 0.86, kappa coefficient is 0.81).

Visual GIS	LCZ 1	LCZ 1A	LCZ 2	LCZ 2A	LCZ 3	LCZ 3A	LCA 3B	LCZ 4	LCZ 4A	LCZ 5	Total Zone	Mapping Accuracy (%)
LCZ 1	2	0	0	0	0	0	0	0	0	0	2	1
LCZ 1A	1	1	1	0	0	0	0	0	0	0	3	33
LCZ 2	0	0	21	0	0	0	0	0	0	0	21	1
LCZ 2A	0	0	1	0	0	1	0	0	0	0	2	0
LCZ 3	0	0	1	0	7	0	0	0	0	0	8	88
LCZ 3A	0	0	0	0	0	4	1	0	0	0	5	80
LCA 3B	0	0	0	0	0	0	2	0	0	0	2	100
LCZ 4	0	0	0	0	0	0	0	1	0	0	1	100
LCZ 4A	1	0	0	0	0	0	0	0	3	0	4	75
LCZ 5	0	0	0	0	0	0	0	0	0	2	2	100
Total Zone	4	1	24	0	7	5	3	1	3	2	50	
Mapping accuracy (%)	50	1	88	0	1	80	66	100	100	100		

Appendix C

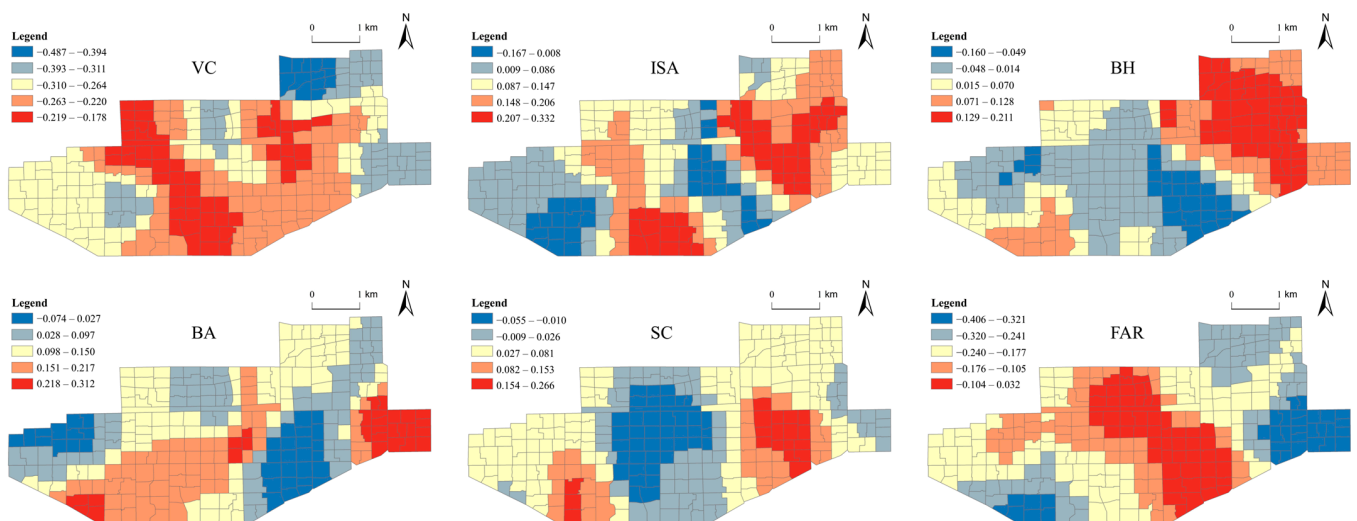


Figure A2. Local regression coefficients of GWR result in 2010.

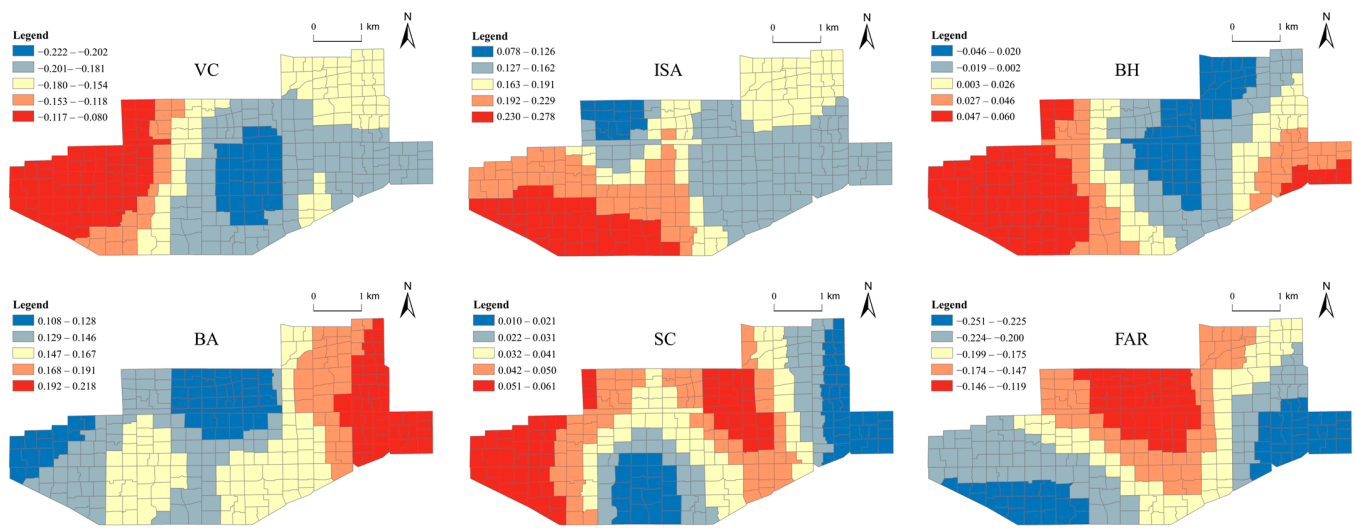


Figure A3. Local regression coefficients of GWR result in 2015.

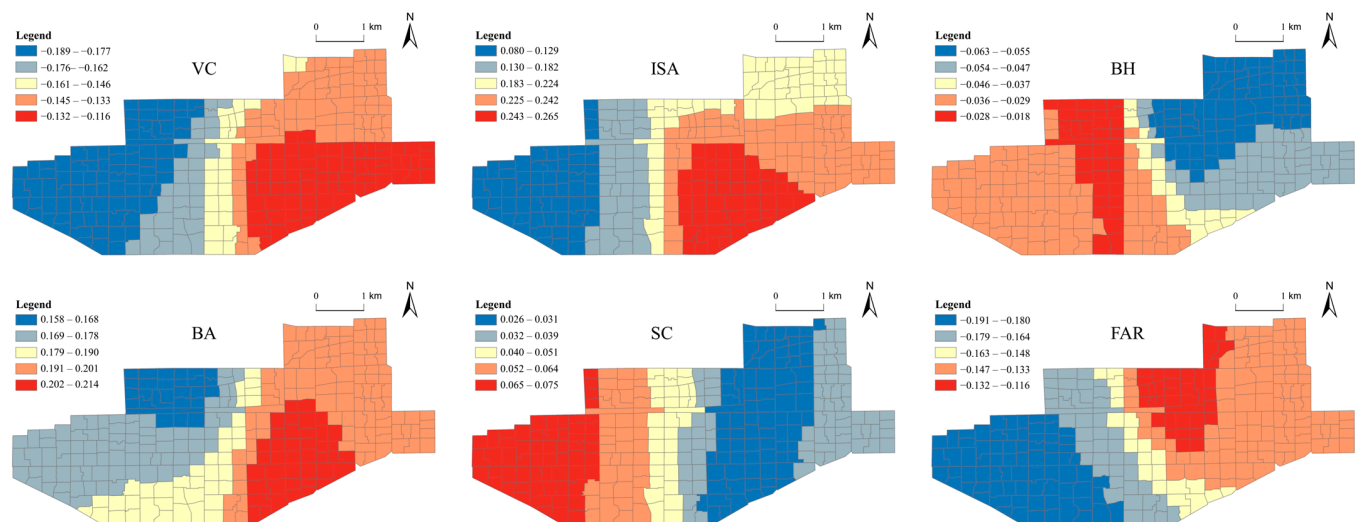


Figure A4. Local regression coefficients of GWR result in 2020.

References

1. IPCC. *Climate Change 2022: Mitigation of Climate Change. Contribution of Working Group III to the Sixth Assessment Report of the Intergovernmental Panel on Climate Change*; Cambridge University Press: Cambridge, UK; New York, NY, USA, 2022.
2. Rizwan, A.M.; Dennis, L.Y.C.; Liu, C. A review on the generation, determination and mitigation of urban heat island. *J. Environ. Sci.* **2008**, *20*, 120–128. [[CrossRef](#)] [[PubMed](#)]
3. Li, X.; Zhou, Y.; Yu, S.; Jia, G.; Li, H.; Li, W. Urban heat island impacts on building energy consumption: A review of approaches and findings. *Energy* **2019**, *174*, 407–419. [[CrossRef](#)]
4. Agarwal, M.; Tandon, A. Modeling of the urban heat island in the form of mesoscale wind and of its effect on air pollution dispersal. *Appl. Math. Model.* **2010**, *34*, 2520–2530. [[CrossRef](#)]
5. Wong, K.V.; Paddon, A.; Jimenez, A. Review of world urban heat islands: Many linked to increased mortality. *J. Energy Resour. Technol.* **2013**, *135*, 022101. [[CrossRef](#)]
6. Shahfahad; Naikoo, M.W.; Towfiqul Islam, A.R.M.; Mallick, J.; Rahman, A. Land use/land cover change and its impact on surface urban heat island and urban thermal comfort in a metropolitan city. *Urban Clim.* **2022**, *41*, 101052. [[CrossRef](#)]
7. Krehbiel, C.P.; Jackson, T.; Henebry, G.M. Web-enabled landsat data time series for monitoring urban heat island impacts on land surface phenology. *IEEE J. Sel. Top. Appl. Earth Obs. Remote Sens.* **2016**, *9*, 2043–2050. [[CrossRef](#)]
8. Weng, Q. Remote sensing of impervious surfaces in the urban areas: Requirements, methods, and trends. *Remote Sens. Environ.* **2012**, *117*, 34–49. [[CrossRef](#)]
9. Mohan, M.; Kandya, A. Impact of urbanization and land-use/land-cover change on diurnal temperature range: A case study of tropical urban airshed of India using remote sensing data. *Sci. Total Environ.* **2015**, *506–507*, 453–465. [[CrossRef](#)]

10. Dai, Z.; Guldmann, J.M.; Hu, Y. Spatial regression models of park and land-use impacts on the urban heat island in central Beijing. *Sci. Total Environ.* **2018**, *626*, 1136–1147. [[CrossRef](#)]
11. Kamali Maskooni, E.; Hashemi, H.; Berndtsson, R.; Daneshkar Arasteh, P.; Kazemi, M. Impact of spatiotemporal land-use and land-cover changes on surface urban heat islands in a semiarid region using Landsat data. *Int. J. Digit. Earth* **2021**, *14*, 250–270. [[CrossRef](#)]
12. Mansour, K.; Aziz, M.A.; Hashim, S.; Effat, H. Impact of anthropogenic activities on urban heat islands in major cities of El-Minya Governorate, Egypt. *Egypt. J. Remote Sens. Space Sci.* **2022**, *25*, 609–620. [[CrossRef](#)]
13. Marković, M.; Cheema, J.; Teofilović, A.; Čepić, S.; Popović, Z.; Tomićević-Dubljević, J.; Pause, M. Monitoring of spatiotemporal change of green spaces in relation to the land surface temperature: A case study of Belgrade, Serbia. *Remote Sens.* **2021**, *13*, 3846. [[CrossRef](#)]
14. Zhu, Z.; Shen, Y.; Fu, W.; Zheng, D.; Huang, P.; Li, J.; Lan, Y.; Chen, Z.; Liu, Q.; Xu, X.; et al. How does 2D and 3D of urban morphology affect the seasonal land surface temperature in Island City? A block-scale perspective. *Ecol. Indic.* **2023**, *150*, 110221. [[CrossRef](#)]
15. Huang, X.; Wang, Y. Investigating the effects of 3D urban morphology on the surface urban heat island effect in urban functional zones by using high-resolution remote sensing data: A case study of Wuhan, central China. *ISPRS J. Photogramm. Remote Sens.* **2019**, *152*, 119–131. [[CrossRef](#)]
16. Zhou, R.; Xu, H.; Zhang, H.; Zhang, J.; Liu, M.; He, T.; Gao, J.; Li, C. Quantifying the relationship between 2D/3D building patterns and land surface temperature: Study on the metropolitan Shanghai. *Remote Sens.* **2022**, *14*, 4098. [[CrossRef](#)]
17. Li, X.; Yang, B.; Xu, G.; Liang, F.; Jiang, T.; Dong, Z. Exploring the impact of 2-D/3-D building morphology on the land surface temperature: A case study of three megacities in China. *IEEE J. Sel. Top. Appl. Earth Obs. Remote Sens.* **2021**, *14*, 4933–4945. [[CrossRef](#)]
18. Kolokotsa, D.; Lilli, K.; Gobakis, K.; Mavrigiannaki, A.; Haddad, S.; Garshasbi, S.; Mohajer, H.R.H.; Paolini, R.; Vasilakopoulou, K.; Bartesaghi, C.; et al. Analyzing the impact of urban planning and building typologies in urban heat island mitigation. *Buildings* **2022**, *12*, 537. [[CrossRef](#)]
19. Elkhazindar, A.; Kharrufa, S.N.; Arar, M.S. The effect of urban form on the heat island phenomenon and human thermal comfort: A comparative study of UAE residential sites. *Energies* **2022**, *15*, 5471. [[CrossRef](#)]
20. Wu, Z.; Tong, Z.; Wang, M.; Long, Q. Assessing the impact of urban morphological parameters on land surface temperature in the heat aggregation areas with spatial heterogeneity: A case study of Nanjing. *Build. Environ.* **2023**, *235*, 110232. [[CrossRef](#)]
21. Gao, Y.; Zhao, J.; Han, L. Exploring the spatial heterogeneity of urban heat island effect and its relationship to block morphology with the geographically weighted regression model. *Sustain. Cities Soc.* **2022**, *76*, 103431. [[CrossRef](#)]
22. Hidalgo-García, D.; Arco-Díaz, J. Modeling the surface urban heat island (SUHI) to study of its relationship with variations in the thermal field and with the indices of land use in the metropolitan area of Granada (Spain). *Sustain. Cities Soc.* **2022**, *87*, 104166. [[CrossRef](#)]
23. Ghosh, S.; Kumar, D.; Kumari, R. Assessing spatiotemporal variations in land surface temperature and SUHI intensity with a cloud based computational system over five major cities of India. *Sustain. Cities Soc.* **2022**, *85*, 104060. [[CrossRef](#)]
24. Deng, X.; Gao, F.; Liao, S.; Liu, Y.; Chen, W. Spatiotemporal evolution patterns of urban heat island and its relationship with urbanization in Guangdong-Hong Kong-Macao greater bay area of China from 2000 to 2020. *Ecol. Indic.* **2023**, *146*, 109817. [[CrossRef](#)]
25. Abd-Elmabod, S.K.; Jiménez-González, M.A.; Jordán, A.; Zhang, Z.; Mohamed, E.S.; Hammam, A.A.; El Baroudy, A.A.; Abdel-Fattah, M.K.; Abdelfattah, M.A.; Jones, L. Past and future impacts of urbanisation on land surface temperature in Greater Cairo over a 45 year period. *Egypt. J. Remote Sens. Space Sci.* **2022**, *25*, 961–974. [[CrossRef](#)]
26. Liu, X.; Ming, Y.; Liu, Y.; Yue, W.; Han, G. Influences of landform and urban form factors on urban heat island: Comparative case study between Chengdu and Chongqing. *Sci. Total Environ.* **2022**, *820*, 153395. [[CrossRef](#)]
27. Gu, Y.; You, X.-y. A spatial quantile regression model for driving mechanism of urban heat island by considering the spatial dependence and heterogeneity: An example of Beijing, China. *Sustain. Cities Soc.* **2022**, *79*, 103692. [[CrossRef](#)]
28. Yu, X.; Xu, G.; Liu, Y.; Xiao, R. Influences of 3D features of buildings on land surface temperature: A case study in the Yangtze River Delta urban agglomeration. *China Environ. Sci.* **2021**, *41*, 5806–5816. [[CrossRef](#)]
29. Cao, S.; Cai, Y.; Du, M.; Weng, Q.; Lu, L. Seasonal and diurnal surface urban heat islands in China: An investigation of driving factors with three-dimensional urban morphological parameters. *GISci. Remote Sens.* **2022**, *59*, 1121–1142. [[CrossRef](#)]
30. Wang, J.; Meng, F.; Lu, H.; Lv, Y.; Jing, T. Individual and combined effects of 3D buildings and green spaces on the urban thermal environment: A case study in Jinan, China. *Atmosphere* **2023**, *14*, 908. [[CrossRef](#)]
31. Liu, Y.; Xu, Y.; Zhang, F.; Shu, W. Influence of Beijing spatial morphology on the distribution of urban heat island. *Acta Geogr. Sin.* **2021**, *76*, 1662–1679. [[CrossRef](#)]
32. Yan, G.; Su, J.; Guan, D. The impact of urban architectural vertical characteristics on urban thermal environment in Zhongshan District, Dalian. *Sci. Geogr. Sin.* **2019**, *39*, 125–130. [[CrossRef](#)]
33. Hou, H.; Su, H.; Yao, C.; Wang, Z. Spatiotemporal patterns of the impact of surface roughness and morphology on urban heat island. *Sustain. Cities Soc.* **2023**, *92*, 104513. [[CrossRef](#)]
34. Zheng, Y.; Ren, C.; Shi, Y.; Yim, S.H.L.; Lai, D.Y.F.; Xu, Y.; Fang, C.; Li, W. Mapping the spatial distribution of nocturnal urban heat island based on local climate zone framework. *Build. Environ.* **2023**, *234*, 110197. [[CrossRef](#)]

35. Yu, X.; Liu, Y.; Zhang, Z.; Xiao, R. Influences of buildings on urban heat island based on 3D landscape metrics: An investigation of China's 30 megacities at micro grid-cell scale and macro city scale. *Landsc. Ecol.* **2021**, *36*, 2743–2762. [[CrossRef](#)]
36. Yang, L.; Yu, K.; Ai, J.; Liu, Y.; Yang, W.; Liu, J. Dominant factors and spatial heterogeneity of land surface temperatures in urban areas: A case study in Fuzhou, China. *Remote Sens.* **2022**, *14*, 1266. [[CrossRef](#)]
37. Kim, J.; Lee, D.K.; Brown, R.D.; Kim, S.; Kim, J.H.; Sung, S. The effect of extremely low sky view factor on land surface temperatures in urban residential areas. *Sustain. Cities Soc.* **2022**, *80*, 103799. [[CrossRef](#)]
38. Lu, H.; Li, F.; Yang, G.; Sun, W. Multi-scale impacts of 2D/3D urban building pattern in intra-annual thermal environment of Hangzhou, China. *Int. J. Appl. Earth Obs. Geoinf.* **2021**, *104*, 102558. [[CrossRef](#)]
39. Chen, Y.; Yang, J.; Yu, W.; Ren, J.; Xiao, X.; Xia, J.C. Relationship between urban spatial form and seasonal land surface temperature under different grid scales. *Sustain. Cities Soc.* **2023**, *89*, 104374. [[CrossRef](#)]
40. Yang, C.; Zhu, W.; Sun, J.; Xu, X.; Wang, R.; Lu, Y.; Zhang, S.; Zhou, W. Assessing the effects of 2D/3D urban morphology on the 3D urban thermal environment by using multi-source remote sensing data and UAV measurements: A case study of the snow-climate city of Changchun, China. *J. Clean. Prod.* **2021**, *321*, 128956. [[CrossRef](#)]
41. Zhang, N.; Zhang, J.; Chen, W.; Su, J. Block-based variations in the impact of characteristics of urban functional zones on the urban heat island effect: A case study of Beijing. *Sustain. Cities Soc.* **2022**, *76*, 103529. [[CrossRef](#)]
42. Wang, Q.; Wang, X.; Meng, Y.; Zhou, Y.; Wang, H. Exploring the impact of urban features on the spatial variation of land surface temperature within the diurnal cycle. *Sustain. Cities Soc.* **2023**, *91*, 104432. [[CrossRef](#)]
43. Hu, Y.; Dai, Z.; Guldman, J.M. Modeling the impact of 2D/3D urban indicators on the urban heat island over different seasons: A boosted regression tree approach. *J. Environ. Manag.* **2020**, *266*, 110424. [[CrossRef](#)] [[PubMed](#)]
44. Han, S.; Hou, H.; Estoque, R.C.; Zheng, Y.; Shen, C.; Murayama, Y.; Pan, J.; Wang, B.; Hu, T. Seasonal effects of urban morphology on land surface temperature in a three-dimensional perspective: A case study in Hangzhou, China. *Build. Environ.* **2023**, *228*, 109913. [[CrossRef](#)]
45. Stewart, I.D.; Oke, T.R. Local climate zones for urban temperature studies. *Bull. Am. Meteorol. Soc.* **2012**, *93*, 1879–1900. [[CrossRef](#)]
46. Wang, R.; Cai, M.; Ren, C.; Bechtel, B.; Xu, Y.; Ng, E. Detecting multi-temporal land cover change and land surface temperature in Pearl River Delta by adopting local climate zone. *Urban Clim.* **2019**, *28*, 100455. [[CrossRef](#)]
47. Zheng, B.; Chen, Y.; Hu, Y. Analysis of land cover and SUHII pattern using local climate zone framework—A case study of Chang-Zhu-Tan main urban area. *Urban Clim.* **2022**, *43*, 101153. [[CrossRef](#)]
48. Yang, J.; Ren, J.; Sun, D.; Xiao, X.; Xia, J.; Jin, C.; Li, X. Understanding land surface temperature impact factors based on local climate zones. *Sustain. Cities Soc.* **2021**, *69*, 102818. [[CrossRef](#)]
49. Zhao, Z.; Sharifi, A.; Dong, X.; Shen, L.; He, B. Spatial variability and temporal heterogeneity of surface urban heat island patterns and the suitability of local climate zones for land surface temperature characterization. *Remote Sens.* **2021**, *13*, 4338. [[CrossRef](#)]
50. Alghamdi, A.S.; Alzhrani, A.I.; Alanazi, H.H. Local climate zones and thermal characteristics in Riyadh City, Saudi Arabia. *Remote Sens.* **2021**, *13*, 4526. [[CrossRef](#)]
51. Geletič, J.; Lehnert, M.; Dobrovolný, P. Land surface temperature differences within local climate zones, based on two central European cities. *Remote Sens.* **2016**, *8*, 788. [[CrossRef](#)]
52. Ochola, E.M.; Fakhrazadehshirazi, E.; Adimo, A.O.; Mukundi, J.B.; Wesonga, J.M.; Sodoudi, S. Inter-local climate zone differentiation of land surface temperatures for management of urban heat in Nairobi City, Kenya. *Urban Clim.* **2020**, *31*, 100540. [[CrossRef](#)]
53. Bechtel, B.; Demuzere, M.; Mills, G.; Zhan, W.; Sismanidis, P.; Small, C.; Voogt, J. SUHI analysis using local climate zones—A comparison of 50 cities. *Urban Clim.* **2019**, *28*, 100451. [[CrossRef](#)]
54. Yang, J.; Wang, Y.; Xiu, C.; Xiao, X.; Xia, J.; Jin, C. Optimizing local climate zones to mitigate urban heat island effect in human settlements. *J. Clean. Prod.* **2020**, *275*, 123767. [[CrossRef](#)]
55. Dian, C.; Pongrácz, R.; Dezső, Z.; Bartholy, J. Annual and monthly analysis of surface urban heat island intensity with respect to the local climate zones in Budapest. *Urban Clim.* **2020**, *31*, 100573. [[CrossRef](#)]
56. Du, P.; Chen, J.; Bai, X.; Han, W. Understanding the seasonal variations of land surface temperature in Nanjing urban area based on local climate zone. *Urban Clim.* **2020**, *33*, 100657. [[CrossRef](#)]
57. Geletič, J.; Lehnert, M.; Savić, S.; Milošević, D. Inter-/intra-zonal seasonal variability of the surface urban heat island based on local climate zones in three central European cities. *Build. Environ.* **2019**, *156*, 21–32. [[CrossRef](#)]
58. Chang, Y.; Xiao, J.; Li, X.; Middel, A.; Zhang, Y.; Gu, Z.; Wu, Y.; He, S. Exploring diurnal thermal variations in urban local climate zones with ECOSTRESS land surface temperature data. *Remote Sens. Environ.* **2021**, *263*, 112544. [[CrossRef](#)]
59. Wang, R.; Voogt, J.; Ren, C.; Ng, E. Spatial-temporal variations of surface urban heat island: An application of local climate zone into large Chinese cities. *Build. Environ.* **2022**, *222*, 109378. [[CrossRef](#)]
60. Eldesoky, A.H.M.; Gil, J.; Pont, M.B. The suitability of the urban local climate zone classification scheme for surface temperature studies in distinct macroclimate regions. *Urban Clim.* **2021**, *37*, 100823. [[CrossRef](#)]
61. Yang, J.; Zhan, Y.; Xiao, X.; Xia, J.C.; Sun, W.; Li, X. Investigating the diversity of land surface temperature characteristics in different scale cities based on local climate zones. *Urban Clim.* **2020**, *34*, 100700. [[CrossRef](#)]
62. Zhou, L.; Yuan, B.; Hu, F.; Wei, C.; Dang, X.; Sun, D. Understanding the effects of 2D/3D urban morphology on land surface temperature based on local climate zones. *Build. Environ.* **2022**, *208*, 108578. [[CrossRef](#)]

63. Hou, X.; Xie, X.; Bagan, H.; Chen, C.; Wang, Q.; Yoshida, T. Exploring spatiotemporal variations in land surface temperature based on local climate zones in Shanghai from 2008 to 2020. *Remote Sens.* **2023**, *15*, 3106. [[CrossRef](#)]
64. Wang, Z.; Zhu, P.; Zhou, Y.; Li, M.; Lu, J.; Huang, Y.; Deng, S. Evidence of relieved urban heat island intensity during rapid urbanization through local climate zones. *Urban Clim.* **2023**, *49*, 101537. [[CrossRef](#)]
65. Azhdari, A.; Soltani, A.; Alidadi, M. Urban morphology and landscape structure effect on land surface temperature: Evidence from Shiraz, a semi-arid city. *Sustain. Cities Soc.* **2018**, *41*, 853–864. [[CrossRef](#)]
66. Liu, H.; Huang, B.; Zhan, Q.; Gao, S.; Li, R.; Fan, Z. The influence of urban form on surface urban heat island and its planning implications: Evidence from 1288 urban clusters in China. *Sustain. Cities Soc.* **2021**, *71*, 102987. [[CrossRef](#)]
67. Wu, Y.; Hou, H.; Wang, R.; Murayama, Y.; Wang, L.; Hu, T. Effects of landscape patterns on the morphological evolution of surface urban heat island in Hangzhou during 2000–2020. *Sustain. Cities Soc.* **2022**, *79*, 103717. [[CrossRef](#)]
68. Wu, Z.; Yao, L.; Zhuang, M.; Ren, Y. Detecting factors controlling spatial patterns in urban land surface temperatures: A case study of Beijing. *Sustain. Cities Soc.* **2020**, *63*, 102454. [[CrossRef](#)]
69. Chen, J.; Du, P.; Jin, S.; Ding, H.; Chen, C.; Xu, Y.; Feng, L.; Guo, G.; Zheng, H.; Huang, M. Unravelling the multilevel and multi-dimensional impacts of building and tree on surface urban heat islands. *Energy Build.* **2022**, *259*, 111843. [[CrossRef](#)]
70. Du, S.; Xiong, Z.; Wang, Y.-C.; Guo, L. Quantifying the multilevel effects of landscape composition and configuration on land surface temperature. *Remote Sens. Environ.* **2016**, *178*, 84–92. [[CrossRef](#)]
71. Liao, W.; Hong, T.; Heo, Y. The effect of spatial heterogeneity in urban morphology on surface urban heat islands. *Energy Build.* **2021**, *244*, 111027. [[CrossRef](#)]
72. Li, Z.; Hu, D. Exploring the relationship between the 2D/3D architectural morphology and urban land surface temperature based on a boosted regression tree: A case study of Beijing, China. *Sustain. Cities Soc.* **2022**, *78*, 103392. [[CrossRef](#)]
73. Yuan, B.; Zhou, L.; Dang, X.; Sun, D.; Hu, F.; Mu, H. Separate and combined effects of 3D building features and urban green space on land surface temperature. *J. Environ. Manag.* **2021**, *295*, 113116. [[CrossRef](#)]
74. Yu, S.; Chen, Z.; Yu, B.; Wang, L.; Wu, B.; Wu, J.; Zhao, F. Exploring the relationship between 2D/3D landscape pattern and land surface temperature based on explainable eXtreme Gradient Boosting tree: A case study of Shanghai, China. *Sci. Total Environ.* **2020**, *725*, 138229. [[CrossRef](#)]
75. Shao, L.; Liao, W.; Li, P.; Luo, M.; Xiong, X.; Liu, X. Drivers of global surface urban heat islands: Surface property, climate background, and 2D/3D urban morphologies. *Build. Environ.* **2023**, *242*, 110581. [[CrossRef](#)]
76. Peng, W.; Wang, R.; Duan, J.; Gao, W.; Fan, Z. Surface and canopy urban heat islands: Does urban morphology result in the spatiotemporal differences? *Urban Clim.* **2022**, *42*, 101136. [[CrossRef](#)]
77. Guo, F.; Wu, Q.; Schlink, U. 3D building configuration as the driver of diurnal and nocturnal land surface temperatures: Application in Beijing's old city. *Build. Environ.* **2021**, *206*, 108354. [[CrossRef](#)]
78. Chen, Y.; Shan, B.; Yu, X. Study on the spatial heterogeneity of urban heat islands and influencing factors. *Build. Environ.* **2022**, *208*, 108604. [[CrossRef](#)]
79. Lu, Y.; Yue, W.; Liu, Y.; Huang, Y. Investigating the spatiotemporal non-stationary relationships between urban spatial form and land surface temperature: A case study of Wuhan, China. *Sustain. Cities Soc.* **2021**, *72*, 103070. [[CrossRef](#)]
80. Hu, D.; Meng, Q.; Schlink, U.; Hertel, D.; Liu, W.; Zhao, M.; Guo, F. How do urban morphological blocks shape spatial patterns of land surface temperature over different seasons? A multifactorial driving analysis of Beijing, China. *Int. J. Appl. Earth Obs. Geoinf.* **2022**, *106*, 102648. [[CrossRef](#)]
81. Liu, H.; Zhan, Q.; Gao, S.; Yang, C. Seasonal variation of the spatially non-stationary association between land surface temperature and urban landscape. *Remote Sens.* **2019**, *11*, 1016. [[CrossRef](#)]
82. Sobrino, J.A.; Jiménez-Muñoz, J.C.; Paolini, L. Land surface temperature retrieval from LANDSAT TM 5. *Remote Sens. Environ.* **2004**, *90*, 434–440. [[CrossRef](#)]
83. Xie, Q.; Liu, J.; Hu, D. Urban expansion and its impact on spatio-temporal variation of urban thermal characteristics: A case study of Wuhan. *Geogr. Res.* **2016**, *35*, 1259–1272. [[CrossRef](#)]
84. Bechtel, B.; Alexander, P.J.; Böhner, J.; Ching, J.; Conrad, O.; Feddema, J.; Mills, G.; See, L.; Stewart, I. Mapping local climate zones for a worldwide database of the form and function of cities. *ISPRS Int. J. Geo-Inf.* **2015**, *4*, 199–219. [[CrossRef](#)]
85. Cai, M.; Ren, C.; Xu, Y.; Lau, K.; Wang, R. Investigating the relationship between local climate zone and land surface temperature using an improved WUDAPT methodology—A case study of Yangtze River Delta, China. *Urban Clim.* **2018**, *24*, 485–502. [[CrossRef](#)]
86. Zheng, Y.; Ren, C.; Xu, Y.; Wang, R.; Ho, J.; Lau, K.; Ng, E. GIS-based mapping of local climate zone in the high-density city of Hong Kong. *Urban Clim.* **2018**, *24*, 419–448. [[CrossRef](#)]
87. Wu, J.; Liu, C.; Wang, H. Analysis of Spatio-temporal patterns and related factors of thermal comfort in subtropical coastal cities based on local climate zones. *Build. Environ.* **2022**, *207*, 108568. [[CrossRef](#)]
88. Quan, S.J.; Dutt, F.; Woodworth, E.; Yamagata, Y.; Yang, P.P.-J. Local Climate Zone Mapping for Energy Resilience: A Fine-grained and 3D Approach. *Energy Procedia* **2017**, *105*, 3777–3783. [[CrossRef](#)]
89. Huang, F.; Jiang, S.; Zhan, W.; Bechtel, B.; Liu, Z.; Demuzere, M.; Huang, Y.; Xu, Y.; Ma, L.; Xia, W.; et al. Mapping local climate zones for cities: A large review. *Remote Sens. Environ.* **2023**, *292*, 113573. [[CrossRef](#)]
90. Liang, S. Narrowband to broadband conversions of land surface albedo I: Algorithms. *Remote Sens. Environ.* **2001**, *76*, 213–238. [[CrossRef](#)]

91. Wang, R.; Ren, C.; Xu, Y.; Lau, K.K.L.; Shi, Y. Mapping the local climate zones of urban areas by GIS-based and WUDAPT methods: A case study of Hong Kong. *Urban Clim.* **2018**, *24*, 567–576. [[CrossRef](#)]
92. Li, Y.; Yin, K.; Wang, Y.; Wang, L.; Yu, Y.; Hu, D. Studies on influence factors of surface urban heat island: A review. *World Sci.-Technol. R D* **2017**, *39*, 51–61. [[CrossRef](#)]
93. Yu, Z.; Yang, G.; Zuo, S.; Jørgensen, G.; Koga, M.; Vejre, H. Critical review on the cooling effect of urban blue-green space: A threshold-size perspective. *Urban For. Urban Green.* **2020**, *49*, 126630. [[CrossRef](#)]
94. Allegrini, J.; Carmeliet, J. Coupled CFD and building energy simulations for studying the impacts of building height topology and buoyancy on local urban microclimates. *Urban Clim.* **2017**, *21*, 278–305. [[CrossRef](#)]
95. Carlson, T.N.; Ripley, D.A. On the relation between NDVI, fractional vegetation cover, and leaf area index. *Remote Sens. Environ.* **1997**, *62*, 241–252. [[CrossRef](#)]
96. Berger, C.; Rosentreter, J.; Voltersen, M.; Baumgart, C.; Schmuilius, C.; Hese, S. Spatio-temporal analysis of the relationship between 2D/3D urban site characteristics and land surface temperature. *Remote Sens. Environ.* **2017**, *193*, 225–243. [[CrossRef](#)]
97. Meng, Q.; Liu, W.; Zhang, L.; Allam, M.; Bi, Y.; Hu, X.; Gao, J.; Hu, D.; Jancsó, T. Relationships between land surface temperatures and neighboring environment in highly urbanized areas: Seasonal and scale effects analyses of Beijing, China. *Remote Sens.* **2022**, *14*, 4340. [[CrossRef](#)]
98. Scarano, M.; Mancini, F. Assessing the relationship between sky view factor and land surface temperature to the spatial resolution. *Int. J. Remote Sens.* **2017**, *38*, 6910–6929. [[CrossRef](#)]
99. Wang, J.; Xu, C. Geodetector: Principle and prospective. *Acta Geogr. Sin.* **2017**, *72*, 116–134. [[CrossRef](#)]
100. Fotheringham, A.S.; Charlton, M.E.; Brunson, C. Geographically weighted regression: A natural evolution of the expansion method for spatial data analysis. *Environ. Plan. A Econ. Space* **1998**, *30*, 1905–1927. [[CrossRef](#)]
101. Shi, Y.; Lau, K.K.L.; Ren, C.; Ng, E. Evaluating the local climate zone classification in high-density heterogeneous urban environment using mobile measurement. *Urban Clim.* **2018**, *25*, 167–186. [[CrossRef](#)]
102. Han, B.; Luo, Z.; Liu, Y.; Zhang, T.; Yang, L. Using local climate zones to investigate spatio-temporal evolution of thermal environment at the urban regional level: A case study in Xi'an, China. *Sustain. Cities Soc.* **2022**, *76*, 103495. [[CrossRef](#)]
103. Federer, C.A. Solar radiation absorption by leafless hardwood forests. *Agric. Meteorol.* **1971**, *9*, 3–20. [[CrossRef](#)]
104. Ma, Q.; Wu, J.; He, C. A hierarchical analysis of the relationship between urban impervious surfaces and land surface temperatures: Spatial scale dependence, temporal variations, and bioclimatic modulation. *Landsc. Ecol.* **2016**, *31*, 1139–1153. [[CrossRef](#)]
105. Sarif, M.O.; Rimal, B.; Stork, N.E. Assessment of changes in land use/land cover and land surface temperatures and their impact on surface urban heat island phenomena in the Kathmandu Valley (1988–2018). *ISPRS Int. J. Geo-Inf.* **2020**, *9*, 726. [[CrossRef](#)]
106. Chen, H.; Deng, Q.; Zhou, Z.; Ren, Z.; Shan, X. Influence of land cover change on spatio-temporal distribution of urban heat island: A case in Wuhan main urban area. *Sustain. Cities Soc.* **2022**, *79*, 103715. [[CrossRef](#)]
107. Moazzam, M.F.U.; Doh, Y.H.; Lee, B.G. Impact of urbanization on land surface temperature and surface urban heat Island using optical remote sensing data: A case study of Jeju Island, Republic of Korea. *Build. Environ.* **2022**, *222*, 109368. [[CrossRef](#)]
108. Bala, R.; Prasad, R.; Yadav, V.P. Quantification of urban heat intensity with land use/land cover changes using Landsat satellite data over urban landscapes. *Theor. Appl. Climatol.* **2021**, *145*, 1–12. [[CrossRef](#)]
109. Feng, X.; Myint, S.W. Exploring the effect of neighboring land cover pattern on land surface temperature of central building objects. *Build. Environ.* **2016**, *95*, 346–354. [[CrossRef](#)]
110. Lan, Y.; Zhan, Q. How do urban buildings impact summer air temperature? The effects of building configurations in space and time. *Build. Environ.* **2017**, *125*, 88–98. [[CrossRef](#)]
111. Chen, Y.; Shan, B.; Yu, X.; Zhang, Q.; Ren, Q. Comprehensive effect of the three-dimensional spatial distribution pattern of buildings on the urban thermal environment. *Urban Clim.* **2022**, *46*, 101324. [[CrossRef](#)]
112. Chen, L.; Ng, E.; An, X.; Ren, C.; Lee, M.; Wang, U.; He, Z. Sky view factor analysis of street canyons and its implications for daytime intra-urban air temperature differentials in high-rise, high-density urban areas of Hong Kong: A GIS-based simulation approach. *Int. J. Climatol.* **2012**, *32*, 121–136. [[CrossRef](#)]
113. Kong, F.; Chen, J.; Middel, A.; Yin, H.; Li, M.; Sun, T.; Zhang, N.; Huang, J.; Liu, H.; Zhou, K.; et al. Impact of 3-D urban landscape patterns on the outdoor thermal environment: A modelling study with SOLWEIG. *Comput. Environ. Urban Syst.* **2022**, *94*, 101773. [[CrossRef](#)]
114. Yang, F.; Lau, S.S.Y.; Qian, F. Summertime heat island intensities in three high-rise housing quarters in inner-city Shanghai China: Building layout, density and greenery. *Build. Environ.* **2010**, *45*, 115–134. [[CrossRef](#)]
115. van Hove, L.W.A.; Jacobs, C.M.J.; Heusinkveld, B.G.; Elbers, J.A.; van Driel, B.L.; Holtslag, A.A.M. Temporal and spatial variability of urban heat island and thermal comfort within the Rotterdam agglomeration. *Build. Environ.* **2015**, *83*, 91–103. [[CrossRef](#)]
116. Yan, H.; Wang, K.; Lin, T.; Zhang, G.; Sun, C.; Hu, X.; Ye, H. The challenge of the urban compact form: Three-dimensional index construction and urban land surface temperature impacts. *Remote Sens.* **2021**, *13*, 1067. [[CrossRef](#)]
117. Lu, L.; Fu, P.; Dewan, A.; Li, Q. Contrasting determinants of land surface temperature in three megacities: Implications to cool tropical metropolitan regions. *Sustain. Cities Soc.* **2023**, *92*, 104505. [[CrossRef](#)]
118. Wang, Q.; Wang, X.; Zhou, Y.; Liu, D.; Wang, H. The dominant factors and influence of urban characteristics on land surface temperature using random forest algorithm. *Sustain. Cities Soc.* **2022**, *79*, 103722. [[CrossRef](#)]

119. Zhang, Z.; Luan, W.; Yang, J.; Guo, A.; Su, M.; Tian, C. The influences of 2D/3D urban morphology on land surface temperature at the block scale in Chinese megacities. *Urban Clim.* **2023**, *49*, 101553. [[CrossRef](#)]
120. Guo, G.; Zhou, X.; Wu, Z.; Xiao, R.; Chen, Y. Characterizing the impact of urban morphology heterogeneity on land surface temperature in Guangzhou, China. *Environ. Model. Softw.* **2016**, *84*, 427–439. [[CrossRef](#)]

Disclaimer/Publisher’s Note: The statements, opinions and data contained in all publications are solely those of the individual author(s) and contributor(s) and not of MDPI and/or the editor(s). MDPI and/or the editor(s) disclaim responsibility for any injury to people or property resulting from any ideas, methods, instructions or products referred to in the content.